

¹ Real-time spectral radiance estimation of hemispherical clear skies ² with machine learned regression models

³ Joseph Del Rocco^{a,*}, Paul D. Bourke^b, Charles B. Patterson^c and Joseph T. Kider^a

⁴ ^a*IST, School of Modeling, Simulation, & Training, University of Central Florida, Orlando, FL, USA*

⁵ ^b*University of Western Australia, Crawley WA, Australia*

⁶ ^c*Full Sail University, Winter Park, FL, USA*

⁷

⁸ ARTICLE INFO

¹¹ **Keywords:**

¹² sky radiance
¹³ spectral radiance
¹⁴ all sky
¹⁵ machine learning
¹⁶ building performance
¹⁷ HDR

¹⁸

¹⁹

²⁰

²¹

²²

²³

²⁴

²⁵

ABSTRACT

Whole sky spectral radiance distribution measurements are difficult and expensive to obtain, yet important for real-time applications of radiative transfer, building performance, physically based rendering, and photovoltaic panel alignment. This work presents a validated machine learning approach to predicting spectral radiance distributions (350–1780 nm) across the entire hemispherical sky, using regression models trained on high dynamic range (HDR) imagery and spectroradiometer measurements. First, we present and evaluate measured, engineered, and computed machine learning features used to train regression models. Next, we perform experiments comparing regular and HDR imagery, sky sample color models, and spectral resolution. Finally, we present a tool that reconstructs a spectral radiance distribution for every single point of a hemispherical clear sky image given only a photograph of the sky and its capture timestamp. We recommend this tool for building performance and spectral rendering pipelines. The spectral radiance of 81 sample points per test sky is estimated to within 7.5% RMSD overall at 1 nm resolution. Spectral radiance distributions are validated against libRadtran and spectroradiometer measurements.

²⁶ 1. Introduction

²⁷ Atmospheric spectral radiance distributions, for ultraviolet (UV), infrared (IR) and visible spectra, for the entire sky,
²⁸ are often simplified into a single downwelling irradiance measurement, mainly because whole sky spectral radiance is
²⁹ difficult and expensive to measure in real-time and complicated to model. Yet precise radiance distributions are still
³⁰ very much needed for accurate calculations in real-time applications of building performance (Hensen and Lamberts,
³¹ 2012; Chandrasekhar, 2013; Jakica, 2017), environmental science (López-Álvarez et al., 2008), photo-voltaic (PV)
³² alignment (Smith et al., 2016), and physically based rendering (Jakob, 2010; Hosek and Wilkie, 2012; Satylmýs et al.,
³³ 2016). Unlike irradiance, spectral radiance is directional and should be available for any point in the sky, as simulations
³⁴ are affected by the angle of incidence of spectral sky energy and receiving surface.

³⁵ We present a data-driven machine learning approach to estimate spectral radiance for any point in a clear sky to
³⁶ within acceptable tolerances for real-time applications. We use high dynamic range (HDR) photographs of the sky
³⁷ and validated spectral radiance measurements captured throughout an entire year by a custom sky scanning framework
³⁸ (Kider et al., 2014), to train models that learn a relationship between capture time, sky appearance, and underlying
³⁹ energy (350–1780 nm). The primary contribution of our research is the reconstruction of high-dimensional atmospheric
⁴⁰ spectral radiance for every single point in a clear sky, including non-visible spectra (UV and near IR), given only a
⁴¹ low-dimensional digital photograph of the sky and its capture time. We show that a clear sky photograph can be used
⁴² to predict non-visible (and visible) atmospheric radiance energy.

⁴³ Notable previous data-driven approaches to model skylight include Tohsing et al. (2014), Saito et al. (2016), and
⁴⁴ López-Álvarez et al. (2008); Cazorla et al. (2008a,b). Tohsing et. al leveraged ground-based sky radiance photographs
⁴⁵ and a non-linear regression model per wavelength to reconstruct only the visible spectrum. Saito et. al used total ozone
⁴⁶ column readings, camera color matching functions, and a linear algebra approach to predict a subset of visible for a
⁴⁷ single point in the sky. Cazorla et al. used neural networks, genetic algorithms, and regression models for specific
⁴⁸ points in the sky. Much of that work was performed on limited sets of data, and in some cases only a few hours of

*Corresponding author.

 jdelrocco@ist.ucf.edu (J. Del Rocco)

ORCID(s):

Nomenclature

$L_{e\Omega\lambda}$	spectral radiance distribution ($\text{W}/\text{m}^2/\text{nm}/\text{sr}$)
$(P\theta, P\phi)$	sky point of interest (azimuth, altitude) ($^\circ$)
$(S\theta, S\phi)$	sun location (azimuth, altitude) ($^\circ$)
(x, y)	sky image pixel coordinate
σ	standard deviation
SPA	sun point angle ($^\circ$)
ETR	extra trees regression model
RFR	random forest regression model
KNR	k-nearest-neighbor regression model
LNR	linear regression model
R^2	coefficient of determination score [-1, 1]
RMSD	root mean squared deviation (%)

49 single sky cover used for training (Tohsing et al., 2014). Our dataset is much more comprehensive. And our methods
 50 predict a wider, more useful spectral range, for every point in the sky. Furthermore, we show the reconstruction of
 51 non-visible energy from photometric inputs.

52 In this work, four separate regression models are developed through machine learning, with a combination of input
 53 features from correlated sky imagery and validated spectral radiance measurements. A series of new experiments are
 54 performed to test model effectiveness and efficiency with regards to changes in exposure, sky sample color model,
 55 and spectrum resolution. A tool is developed that uses a single model to predict spectral radiance distributions for
 56 every point of a hemispherical sky, at 1 nm resolution. Spectral radiance distributions are validated against libRadtran,
 57 a validated radiative transfer software package for atmospheric science (Emde et al., 2016; Buras and Mayer, 2011;
 58 Mayer and Kylling, 2005; Kylling et al., 1995; Dahlback and Stamnes, 1991; Stamnes et al., 1988).

59 We explain in Subsection 3.1 that this work focuses on clear skies by design. In our initial work (Del Rocco et al.,
 60 2018), we showed that regression models were not the best solution for scattered and overcast skies, despite the fact
 61 that one of the models showed promise. We believe a more complex machine-learning solution is needed to understand
 62 the more complicated patterns behind cloudy sky radiance. In contrast to more traditional atmospheric models, we
 63 purposely omit aerosol optical depth (AOD) and trace gas measurements to test viability of our methods today in
 64 real-time applications (commodity building monitoring systems, residential solar installations, rendering pipelines,
 65 etc.), which often do not have access to accurate sky measurements needed for complex physically-based solutions.
 66 Our proposed methods can accommodate readily available AOD and other atmospheric measurements as training and
 67 prediction features. Such features may even help our models adapt to localized turbidity.

68 The remainder of this paper is organized as follows. First, related work is presented in Section 2. Our measurements
 69 and engineered data is detailed in Section 3. We present our methods and experiments in Section 4, results in Section 5,
 70 and validations in Section 6. Finally, conclusions and future work are presented in Section 7.

71 2. Related work

72 Skylight itself has been studied for well over one hundred years (Strutt, 1871; Mie, 1908). Skylight simulation
 73 models typically fall into one of three categories. Early work often simplified solar and sky models by simulating lu-
 74 minance distributions and salient color characteristics with simple analytical equations. Later, the atmospheric science
 75 and computer graphics communities, separately and simultaneously, proposed brute-force physically-based simulations
 76 of light transport in the atmosphere using the radiative transfer equation (RTE) (Chandrasekhar, 1950; Mishchenko
 77 et al., 2002; Chandrasekhar, 2013). More recently, in the “big data” era, some researchers have attempted to model
 78 skylight with data-driven approaches, which often measure, process, and quantify large sets of data and search for cor-
 79 relations, usually with machine learning approaches. Modern atmospheric measuring systems installed at labs around
 80 the world are powerful and accurate, but often expensive and slow, and thus commodity sky scanning systems are more

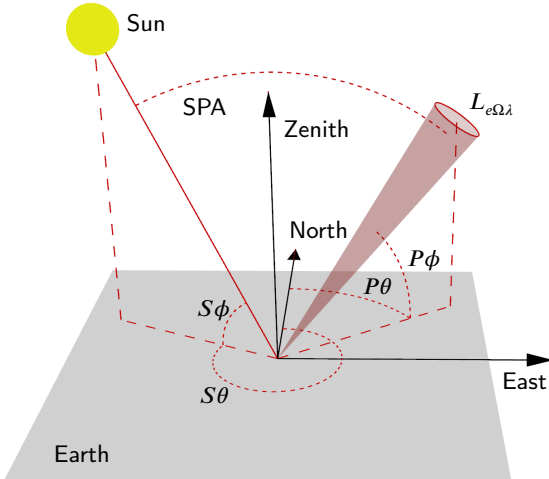


Figure 1: This figure explains the coordinate space and sky coordinates of measurements used in this work. A single atmospheric spectral radiance measurement ($L_{e\Omega\lambda}$) is measured at sky coordinates ($P\theta, P\phi$) (azimuth, altitude), taken from the ground by a custom sky scanning system. 81 such measurements were taken per sky capture. The sky coordinates of the sun ($S\theta, S\phi$) were computed with NREL's solar position algorithm. The central angle between sun location and sky point of interest is denoted as sun-point-angle (SPA) (Chauvin et al., 2015).

81 feasible for modern building performance solutions needed today (Butler, 2008; Mazria and Kershner, 2008).

82 **2.1. Analytical methods**

83 Analytical skylight models fit parametric functions to observations of the sky (Pokrowski, 1929; Kittler, 1994).
 84 Such models were standardized by The International Commission on Illumination (CIE) to calculate the spatial dis-
 85 tribution of skylight, and are based on measurements of luminance, indirect sky irradiance, and direct solar radiance.
 86 Early analytical approaches include the Intermediate Sky by Nakamura et al. (1985) and the UK Building Research
 87 Establishment (BRE) average sky by Littlefair (1981). Lee Jr (2008) studied overcast skies to find meridional consis-
 88 tencies. Cordero et al. (2013) studied albedo effect on radiance distributions (both upwelling and downwelling). One
 89 of the most popular analytical models is the all-weather model by Perez et al. (1993), which formulated a mathemat-
 90 ical equation with five coefficients to model sky luminance. This model was extended by Preetham et al. (1999) to
 91 calculate sky color values by fitting equations to a brute-force physically-based simulation. Hosek and Wilkie (2012)
 92 made several improvements including ground albedo, more realistic turbidity, and the handling of spectral compo-
 93 nents independently. Igawa and Nakamura (2001) and Yao et al. (2015) also improved the Perez all-sky model. All of
 94 these models produce realistic looking results, but often suffer from inaccuracies (Zotti et al., 2007; Kider et al., 2014;
 95 Bruneton, 2016).

96 **2.2. Physically-based methods**

97 Physically-based skylight methods produce the highest quality results of simulating skylight. They directly calcu-
 98 late the transfer of solar radiation in the atmosphere through the radiative transfer equation (RTE). They also directly
 99 calculate the composition of the atmosphere through Rayleigh and Mie scattering, and polarization. The atmospheric
 100 research community developed programs such as 6SV (Vermote et al., 2006), SMARTS2 (Gueymard et al., 1995),
 101 MODTRAN (Berk et al., 2014), and SBDART (Ricchiazzi et al., 1998), which produce accurate results, but often at
 102 high computational cost unsuitable for real-time applications. They also tend to focus on luminance and irradiance.
 103 libRadtran (Emde et al., 2016; Mayer and Kylling, 2005) is a popular, validated software package with various RTE
 104 solvers for atmospheric spectral radiance, irradiance, and other solar and sky properties, and is highly configurable. We
 105 use it to validate our model predictions. Like all physically-based solutions, libRadtran requires aerosol and particulate
 106 parameters and distributions (Hess et al., 1998; Holben et al., 1998) describing the sky, to produce the most accurate
 107 simulations. An alternative physically-based approach involves even more intricate, though perhaps even more acc-
 108 curate, multi-scattering calculations to reconstruct spectral radiance across varying sky covers (Kocifaj, 2015, 2012,

109 These calculations require accurate atmospheric measurements. Separately, the computer graphics community
 110 also has developed numerous Monte Carlo based approaches (Nishita et al., 1993, 1996; Haber et al., 2005; Jarosz,
 111 2008) that merge the RTE with the rendering equation (Kajiya, 1986). These methods produce pleasing visual results
 112 and often approximate the complicated scattering calculations with phase substitutions by Henyey and Greenstein
 113 (1941) or Cornette and Shanks (1992).

114 2.3. Data-driven methods

115 In an increasingly “big data” era, where storage is cheap and data volume, velocity, and variety continues to increase
 116 exponentially, many scientists have taken a data-driven approach to solving problems (Gandomi and Haider, 2015;
 117 Sagiroglu and Sinanc, 2013; Chen et al., 2012; Laney, 2001). For modeling skylight, scientists systematically gather
 118 measurements and apply search algorithms to help model and simulate. This includes the capturing of high dynamic
 119 range (HDR) imagery (Stumpfel et al., 2004), image-based lighting, and irradiance and radiance measurements, to
 120 estimate luminance values for the sky directly from captured photographs.

121 The most relevant work to our own comes from Tohsing et al. (2014), the most comprehensive data-driven approach
 122 to date, who used 1143 separate machine learned regression models (one per color component (RGB) per wavelength
 123 of the visible spectrum (380-760 nm)) to estimate whole sky radiance. The authors trained and tested clear and cloudy
 124 skies separately and the entire dataset was captured over a period of 12 days. 113 samples from a 3.5 hour window of a
 125 single clear sky day were used for training. Whole sky scans took 12 minutes to complete, and thus a synthetic image
 126 was used for color sampling. Our data capture was much more comprehensive, spanning an entire year, accounting
 127 for seasonal variation. Skies were captured under 3 minutes, avoiding synthetic imagery (Del Rocco et al., 2018). Our
 128 methods predicts a much wider spectrum of energy (350-1780 nm), including some UV and IR, which is useful for a
 129 variety of applications. We also provide predictions for every single point in a hemispherical sky image. Finally, as
 130 opposed to a system of 1143 regression models, a single regression model is used to predict.

131 Saito et al. (2016) improved upon the work of Sigernes et al. (2008) to estimate sky radiance, specifically “*without*
 132 *any training sets*,” by using an equation of total ozone column and raw sky image red-green-blue (RGB) counts. They
 133 focused on the zenith of the sky (single point) and estimated spectral radiance for a subset of visible wavelengths (430-
 134 680 nm). They too treat clear and cloudy skies separately. A notable contribution is the color matching functions,
 135 which took into account camera lens wavelength dependence, vignetting, and CMOS noise, and were used for cloud
 136 detection in Saito and Iwabuchi (2016). This method should be scaled to include every single point of a sky image,
 137 both clear and cloudy, and validated against a radiative transfer package.

138 Artificial neural networks (ANN), genetic algorithms, and pseudoinverse linear regression models were used in
 139 various projects by López-Álvarez et al. (2008); Cazorla et al. (2008a,b). They also used a custom sky scanner. Their
 140 models focused on visible spectra with a final dataset of 40 samples. More recently, Satylmýs et al. (2016) used an
 141 ANN to model certain properties of skylight.

142 Chauvin et al. (2015) used a custom sky imaging framework for irradiance and cloud detection for the purposes of
 143 concentrating solar plant technology. A noted contribution was their observation of the importance of the circumsolar
 144 region, in opposition of many sky models, and the central angle between sun position and sky point of interest, or
 145 sun-point-angle (SPA). Their research was used for intrahour forecasting to improve solar resource acquisition (Nou
 146 et al., 2018).

147 Our research: (1) reconstructs the spectral radiance of the sky utilizing high resolution imagery, (2) accounts for
 148 seasonal and datetime variation with captures throughout an entire year, (3) accounts for fisheye lens warp, (4) predicts
 149 a wide, useful spectrum of energy (350-1780 nm) at 1 nm resolution, (5) predicts non-visible spectrum energy with
 150 indirect visible data (a novelty), (6) does so for an entire hemispherical clear sky image, (7) tests multiple exposure
 151 imagery, color model, and spectral resolution, (8) considers real-time constrained downstream applications of this
 152 work, (9) trains and compares multiple regression models, and (10) validates spectral radiance predictions against a
 153 modern atmospheric radiative transfer software package.

154 3. Measurements and data

155 Measurements in this work come from the sky scanner discussed in detail by Kider et al. (2014). This framework
 156 captured high-resolution HDR imagery of the sky (8 exposures), along with atmospheric spectral radiance distributions
 157 (350-2500 nm) from 81 sample points in concentric circle patterns across the sky. Measurements were taken from the
 158 ground. The sampling pattern is arbitrary, but was designed to capture a uniformly distributed “skeleton” of measure-

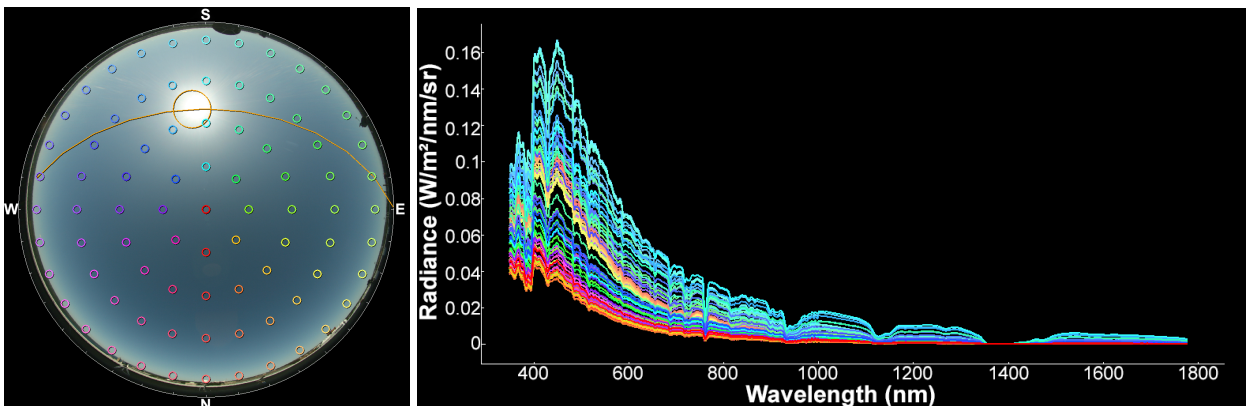


Figure 2: A single sky capture consisted of high-resolution imagery and 81 spectral radiance measurements between 350-2500 nm (350-1780 nm used for this work). (a) shows the sky coordinate locations of the 81 radiance measurements projected onto a sky image; in other words, where in the sky each measurement was made. The sun's location and path is depicted in orange. (b) shows the correlating radiance measurement values in $\text{W} / \text{m}^2 / \text{nm} / \text{sr}$ between 350-1780 nm. The colors of each sky location in (a) correlate with radiance distributions in (b). As expected, radiance measurements taken closer to the sun are higher. The radius of colored circles is not to exact scale with sampled pixel area used in methods described in this work.

ments across the sky. The spectral radiance distributions were measured in $\text{W} / \text{m}^2 / \text{nm} / \text{sr}$ with an ASD FieldSpec Pro spectroradiometer through a 1° solid angle fore-optic (Malthus and MacLellan, 2010), and were validated against NASA datasets (Kider et al., 2014). The multiple exposure photographs of the sky were captured in both CR2 (raw) and JPG formats consecutively at 4368 x 2912 pixels with a commodity Canon 5D digital single-lens reflex (DSLR) full-frame camera with underlying complementary metal-oxide-semiconductor (CMOS) image sensor, together with a Sigma 8 mm f/3.5 EX DG circular fisheye lens, and a Kodak Wratten neutral density filter. JPG compression quality level was set to 100. We automated the process with libgphoto2, which took approximately 40 s to capture all exposures and formats of photographs of the sky. Irradiance was also measured, but ignored for the purposes of this work.

All measurements were taken at a single site location, (42.44344, -76.48163) decimal degrees, on the rooftop of Frank Rhodes Hall, Cornell University, Ithaca, New York, USA. 453 total sky captures were taken over 16 days between 2012-2013, covering all four seasons, dawn to dusk, and various sky covers, for a total of over 36000 individual spectral radiance measurements. Roughly 25% of the captures consisted of full clear skies (0 octas of clouds), from which 6006 individual clear sky samples were used for this work. Scattered and overcast skies were purposely left out of this work to focus our efforts. A complete table listing of all usable data that we captured can be found in Del Rocco et al. (2018). This dataset is freely available to the public through the project website.¹

Hemispherical sky coordinates are specified in (azimuth, altitude) coordinates, where azimuth is an angle Eastward from North, and altitude is (90° – zenith). Sky imagery is vertically flipped due to capture orientation. The correlation of validated radiance measurements and sky color at the same sky coordinates is explained in Subsection 3.2 and Subsection 3.3.

3.1. Sky cover

As mentioned, our entire dataset includes a variety of sky cover conditions, roughly 25% clear skies, 67% scattered, and 8% completely overcast. We assessed sky cover manually with our dataset browsing tool, even though procedural assessment is possible. We used the categorization of sky conditions provided by the US National Oceanic and Atmospheric Administration (NOAA) (Office Of The Federal Coordinator For Meteorological Services And Supporting Research, 2017), designating skies as clear (CLR), scattered (SCT), and overcast (OVC). CLR and OVC skies contained 0 and 8 oktas of cloud cover, respectively. We used SCT for any sky with cloud coverage between 1-7 oktas. The distinction of few (FEW) and broken (BKN) skies was ignored to minimize the number of machine learning models necessary for downstream applications.

As discussed in our preliminary work (Del Rocco et al., 2018), we initially trained and tested sky samples of all

¹ <https://github.com/spectralskylight>

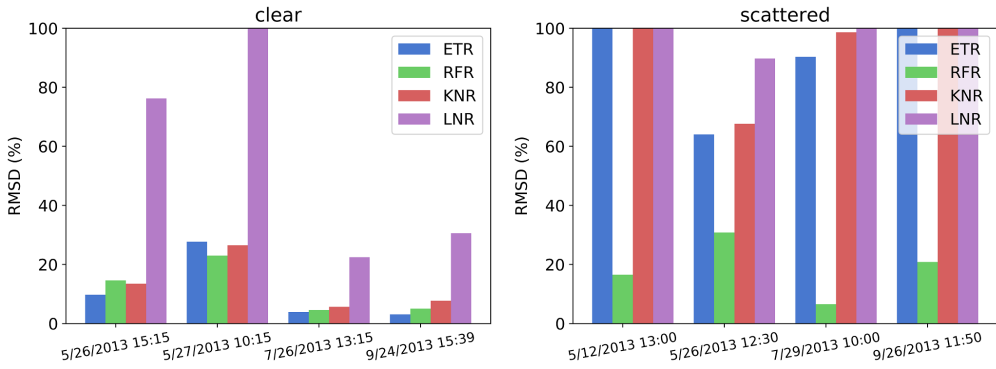


Figure 3: Preliminary results on sky cover specific datasets from Del Rocco et al. (2018). In general, our proposed method performs better on clear skies. One of our models showed promise on scattered cloudy skies, but we focus on clear skies for this work.

188 sky covers. We then found that our regression models performed dramatically better when tested on sky cover specific
 189 datasets. Although we were able to show that at least one regression model performed admirably well on scattered
 190 skies, we surmised for the time being that perhaps more complicated models (e.g. deep learning neural networks) were
 191 best suited to model the likely non-linear relationships of scattered and overcast skies and spectral radiation. Therefore
 192 the work proposed here is our most refined approach of using regression models on clear skies specifically. This
 193 includes validation of our predictions with a validated radiative transfer software package, more experiments, spectral
 194 radiance predictions for every single pixel of a sky photo, the use of multiple exposures (HDR), the accommodation
 195 of lens linearity, sky samples within the circumsolar region, and more accurate whole sky error plots.

196 As the title of this work suggests, the regression model approach presented is currently not unified across all sky
 197 covers. The process of separating clear, scattered, and overcast skies has been discussed in many prior papers, using
 198 metrics such as clear-sky index, R/B ratio, fractional cloud cover, colorimetric and spectral combined metric, etc.
 199 (Arking and Childs, 1985; López-Álvarez et al., 2008; Cazorla et al., 2008b; Yamashita et al., 2004; Li et al., 2011;
 200 Saito and Iwabuchi, 2016; Nou et al., 2018). There are two valid procedural approaches to using our models. Either
 201 categorize the entire sky into buckets of CLR, FEW, BKN, SCT, OVC (or any other distinction), and use a capture of
 202 the sky with an appropriate model, or separate clear from cloudy samples from parts of each sky and pass samples to
 203 separate models for prediction.

204 3.2. Lens linearity

205 Because our work involved mapping hemispherical sky coordinates to 2D pixel coordinates, and vice versa, it
 206 was important to accurately model the behavior of the fisheye lens employed. In a perfect circular fisheye lens, often
 207 called a "tru-theta" lens, equal increments in radius on the fisheye image correspond to equal angle increments of the
 208 respective field rays. Actual fisheye lenses typically exhibit some form of non-linearity, even those lenses designed to
 209 be linear (Bourke, 2016). Although more important with variegated skies (scattered, overcast, etc.), a measurement
 210 difference of even a single degree can result in sampling pixels in or out of the sun's corona. The standard ideal lens
 211 equation for mapping hemispherical sky coordinates to 2D center offset coordinates can be written as:

$$(x, y) = \frac{2 \cdot \text{zenith}}{\text{fisheyefov}} \cdot (\cos(\text{azimuth}), \sin(\text{azimuth})). \quad (1)$$

212 The following procedure was used to measure the relationship between field angle and position on the image:

- 213 1. A close and distant vertical feature in the fisheye image was chosen. The zero parallax position of the lens is the
 214 position along the lens axis where those features stay aligned despite rotations perpendicular to the lens axis.
- 215 2. A clear narrow object in the image was chosen as a reference point and aligned with the center of fisheye image.
- 216 3. The lens is rotated in 5° steps from 0 to 90°, and a photograph taken.
- 217 4. For each photograph, the distance of the reference point from the center was measured.

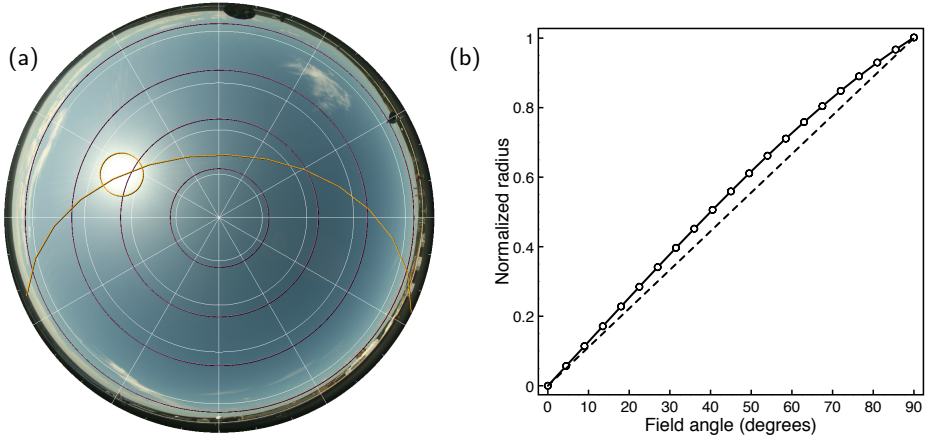


Figure 4: This figure visualizes the linearity of our lens, or the differences ("lens warp") between an ideal fisheye lens and the lens we used in this work. (a) plots the altitudes 12.1151° , 33.749° , 53.3665° , and 71.9187° (altitudes of radiance measurements) for our actual lens (magenta) vs an ideal fisheye lens (white). The deviation, in terms of number of pixels, is not insignificant. The computed location and path of the sun, after lens correction, is overlaid (orange). (b) plots sample points from a lens linearity calibration experiment from our actual lens (solid line) vs an ideal fisheye lens (dashed line). The sample points of the solid line were used to fit Eq. 2.

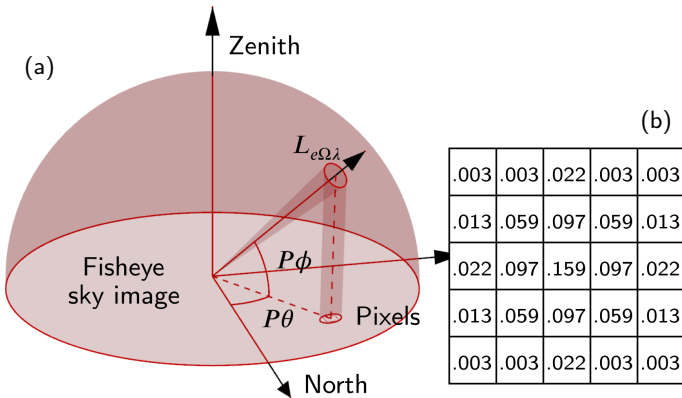


Figure 5: Here we show the standard radiometry of measuring the steridian area of a single sky sample, one of 81 spectral radiance measurements at sky coordinate $(P\theta, P\phi)$ (azimuth, altitude), whose coordinate is then projected onto a 2D photo of the sky. (a) shows the captured steridian area projected onto the sky image, the bounds of which contain the pixels of interest for that sky sample; (b) shows the weights of a 5×5 Gaussian convolution matrix which is applied to the pixels in those bounds to compute a final color for that sky sample.

218 For our Sigma 8 mm f/3.5 fisheye lens, this resulted in the following non-linear curve (plotted in Fig. 4), which was
 219 then used to alter zenith of sky coordinates ($r = \text{zenith}$):

$$r' = 0.7230r + 0.0252r^2 - 0.0499r^3 - 0.0004325r^4. \quad (2)$$

220 3.3. Sky color sampling

221 Color at a particular location in the sky is a fairly subjective measure. What our eyes detect, what instruments
 222 measure, and how that data is processed, differs dramatically. Nevertheless, our research investigates the relationship
 223 between sky color and energy distribution, and thus a quantitative metric must be used.

224 To quantify sky color at specific points in the sky, we projected the bounds of a 1° solid angle (same as fore-optic
 225 we used when measuring radiance) onto the 2D sky images captured with our digital camera (multiple images for the

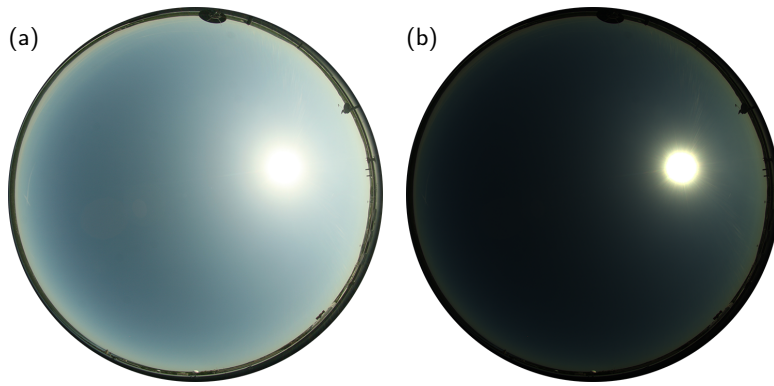


Figure 6: 05/27/2013 09:00 1s exposure of sky as a more traditional, camera processed, compressed JPG (a), and as a minimally processed, uncompressed TIFF (b). (a) approximates what humans see when looking at the sky, but (b) is more accurate in terms of what the DSLR CMOS sensor measures.

226 HDR experiment), and then sampled the pixel colors with a square convolution of similar width to the radius (Fig. 5).
 227 In other words, when exporting data associated with a sky capture, we correlate the 81 radiance measurements with
 228 81 pixel samplings of a sky photo, at the same lens linearity corrected coordinates projected to 2D.

229 More than a single pixel was used to estimate sky color at each sampled sky location because the corresponding
 230 spectral radiance measurement was captured within a 1° steridian. To estimate the equivalent color, we used a common
 231 image processing technique known as convolution, which involves sliding a matrix of weights or homogeneous values
 232 (the kernel) over a set of image pixels in order to compute a new set of pixels (Parker, 2010). Such convolutions are
 233 used to implement a wide variety of image filters like blurring, edge highlighting, etc. We used a Gaussian convolution,
 234 in particular, to blend the pixel colors together, weighting pixels closer to the center higher than pixels near the edges
 235 of the projected bounds.

236 We note that a square convolution does not account for all pixels in a projected circular area exactly; in fact, the
 237 projected circle becomes an increasingly oblong ellipse as altitude decreases. A rectangular convolution kernel would
 238 likely provide better coverage of the pixels in the projected bounds. Our kernel was chosen for real-time efficiency and
 239 overlap with existing image processing techniques and libraries, most of which use square kernels. The weights of our
 240 Gaussian kernels were generated with the following equation (Fisher et al., 1996):

$$\text{kernel}(x, y) = \frac{1}{2\pi\sigma^2} \cdot e^{-\frac{x^2+y^2}{2\sigma^2}}, \quad (3)$$

241 with kernel dimensions relative to the bounds of the convolution, and a standard deviation (σ) of half the radius.

242 3.4. Raw vs. digital positive

243 As mentioned, we captured photographs in a Canon CR2 (raw) format and a more traditional, camera processed,
 244 compressed JPG file format. Raw images contain much more capture information in a pre-interpolated format, before
 245 debayering, noise filtering, color space conversions, gamma correction, etc. In our previous work, we worked with the
 246 compressed JPG captures, which were smaller and faster to process (Del Rocco et al., 2018). For this work, we strove
 247 for accuracy of recorded color values and interpolated the raw photographs into uncompressed TIFF files, using camera
 248 white balance, but no other post-processing options that digital cameras use to produce images closer to what humans
 249 see (e.g. gamma correction, additive brightness, exposure shift, etc.). We used rawpy to read and process the raw
 250 images (Riechert, 2018; LibRaw). Fig. 6 shows the difference. Our previous work already showed that it is possible to
 251 infer a relationship between sky appearance and spectral radiance using compressed imagery. The consistency of raw
 252 photograph interpolation may be more crucial than the specific parameters used.

253 4. Methods and experiments

254 The research question for this work asks whether it is possible (or not) to estimate the atmospheric radiance distri-
 255 bution of a clear sky given only a picture of said sky and its capture timestamp. In other words, is there a relationship

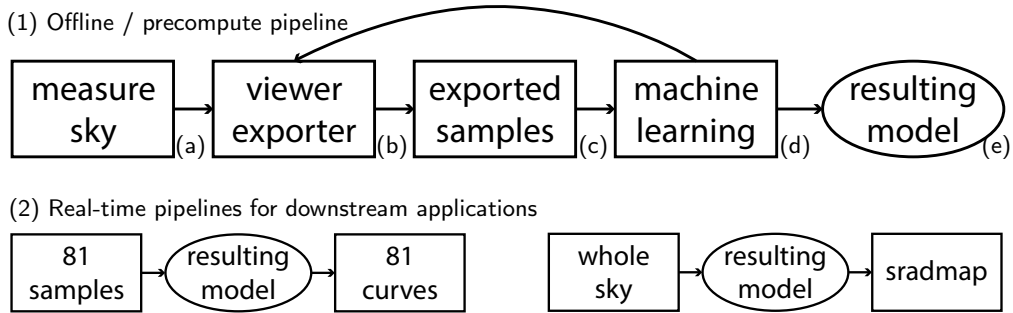


Figure 7: Our method is split into two parts, (1) offline learning to produce a model for (2) real-time application use. (a) is described in Kider et al. (2014). (b) is our viewer/exporter tool used to correlate, inspect, and export datasets. (c) is the clear sky dataset used for this work; each sample of which contains the features depicted in Fig. 8. (d) consists of the methods described in Section 4. While testing on the non-holdout portion of our dataset, identifying data anomalies, incorporating lens linearity equations and adding engineered features, resulted in data being reexported. (e) represents one of our four final regression models produced from this work. In (2), the input features of 81 sky samples from each of our four holdout test skies (Table 1) are passed through a model to predict spectral radiance distribution, which are compared to their corresponding ground truth measurements to produce error plots and validated against libRadtran. Finally, a whole sky image can be passed through a model to produce a spectral radiance map (sradmap), where each “pixel” is a spectral radiance distribution.

256 between what a commodity camera sees in the sky, the time of day, and the underlying spectral energy, despite the
 257 fact that we know solar radiation scattering is a complex process where energy is absorbed and scattered by atmo-
 258 spheric particles at certain wavelengths? Is it possible for mere photos of the sky to give acceptable/useful estimates
 259 of energy for use in downstream applications? In this work, we propose a data-driven method (machine learning on a
 260 dataset of measurements) to help us search for such a relationship. But given the sheer magnitude of machine learning
 261 approaches (statistical models, artificial neural networks, support vector machines, etc.), we limit the scope of this
 262 research to regression models. Predicting a curve (i.e. not a single output) is more of a regression problem, as opposed
 263 to classification or clustering.

264 A supervised approach is natural, given our measurements and problem formulation. Given photos of skies, their
 265 capture timestamp, and 81 corresponding spectral radiance measurements (curves/distributions) per sky, is there a
 266 correlation? The radiance measurements are natural ground truths for what a camera sees at those 81 points in the
 267 sky. As mentioned, we focused on clear sky measurements, specifically 6006 samples (or ~17% of our entire data set),
 268 where each sample represented a single point in a clear sky coupled with capture timestamp and corresponding spectral
 269 radiance measurement. In our initial approach (Del Rocco et al., 2018), we culled all samples within a 20° circumsolar
 270 region, like prior authors Saito et al. (2016) and Tohsing et al. (2014). The work of Chauvin et al. (2015) , who
 271 investigated the radiance profile within the circumsolar region, encouraged us to use all valid sky samples. Samples
 272 closer to the sun are important, as the bulk of energy comes from this area of the sky.

273 We developed a viewer / exporter / converter tool to manage our large dataset and export subset collections of data
 274 (Del Rocco et al., 2018) and (Fig. 7(1b)). Our collection of exported clear sky samples was then partitioned into an
 275 80:20 train/test:holdout ratio, where samples from four arbitrary skies (Table 1), selected at random, were kept in the
 276 holdout partition. The train/test partition was then randomized with the same pseudorandom seed to keep the training
 277 and testing data consistent across runs, and 10-fold cross-validation was utilized to allow us to divide this partition into
 278 training and testing separately while tuning the models. It was also used to dampen the effects of outliers on subsets
 279 of data (Picard and Cook, 1984; Kohavi et al., 1995). At no point in the tuning of models was the holdout data used
 280 for testing. These techniques are often employed to help minimize overfitting and data leakage.

281 Each sky sample of Fig. 7(1c) consisted of a vector of input and output features. From the raw measurements of
 282 capture timestamp, sample azimuth and altitude, sky color, and spectral radiance measurement, we engineered and
 283 computed the additional features: sun azimuth and altitude, sun-point-angle (SPA), quarter, month, week, day and
 284 hour. The capture timestamp was initially included as a single integral feature, but was later “binned” (Macskassy and
 285 Hirsh, 2003) into discrete datetime groupings to help the models better account for seasonal and diurnal variation in
 286 clear sky turbidity (Eltbaakh et al., 2012). Sun position was computed with the solar position algorithm provided by

Table 1

Four holdout test skies selected at random. Table of all measurements listed in Del Rocco et al. (2018)

Date	Time	Part of Day	Season	Sky Cover
05/26/2013	15:15	Afternoon	Spring	CLR
05/27/2013	10:15	Morning	Spring	CLR
07/26/2013	13:15	Midday	Summer	CLR
09/24/2013	15:39	Afternoon	Fall	CLR

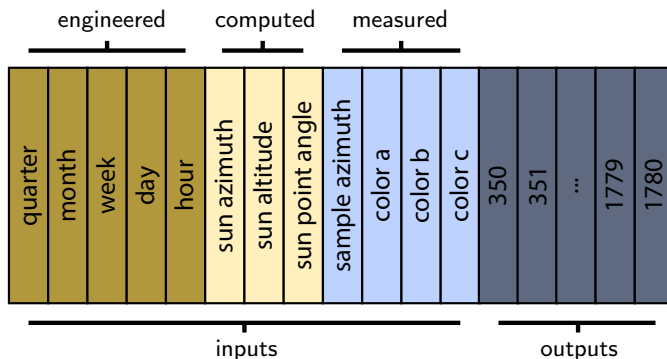


Figure 8: A single sky sample consists of 12 input features and 1430 output features (the spectral radiance curve between 350–1780 nm). Capture timestamp was binned into separate features to help capture seasonal variation. Sun azimuth and altitude were computed via NREL sun position algorithm. Sample azimuth and altitude were inherent to sky scanning logic, yet EDA found them to be of little importance. The three color features are components of single sky color per sample, relative to color model used (e.g. RGB, HSV, etc.).

287 the US National Renewable Energy Laboratory (NREL) (Reda and Andreas, 2004). SPA comes from the insights of
 288 Chauvin et al. (2015), and was not included in our initial work.

289 Various exploratory data analysis (EDA) techniques (Fig. 9) were employed to gauge the significance of each
 290 possible input feature, including: histograms, correlation matrix, collinearity matrix, outlier detection, and feature
 291 importance (Yu, 1977). EDA scores are univariate and calculated by scikit-learn directly (Pedregosa et al., 2011). For
 292 correlation and collinearity, in general, the more correlated input features are to the output, the better they will perform
 293 as predictors, but the more correlated they are to each, the more overlap. F-measure (f-score) is the ratio of harmonic
 294 mean precision and recall, often used as a prediction effectiveness measure, is well documented in statistics literature,
 295 and included in most machine learning libraries (Cooper, 1973; Van Rijsbergen, 1979; Chinchor, 1992; Sasaki, 2007;
 296 Pedregosa et al., 2011).

297 As Fig. 9 shows, all datetime features are naturally correlated, but equally important. By binning the datetime,
 298 we hope the model captures seasonal and time of day variation, which has been shown to affect turbidity ((Eltbaakh
 299 et al., 2012)). The three components of a single color sample (a Gaussian convolution of pixels within a 1° portion
 300 of the sky) are also naturally highly correlated. The hour of day feature likely correlates to sun azimuth more than
 301 altitude because on a 2D projected fisheye photo of the sky, the sun's azimuth varies more than its altitude. Sky sample
 302 color components were found to be the most important features. When HDR data was investigated, longer (brighter)
 303 exposures were found to be more significant than shorter (darker) exposures. Initially, sample azimuth and altitude
 304 were of some importance, but after SPA was added, both sample azimuth and altitude scored as much less important,
 305 likely because SPA is a combination of both sun and sample locations in a single feature. The sample altitude feature
 306 was dropped completely. Sample azimuth was retained because tests without it affected results slightly (~2% RMSD).
 307 As Fig. 9(c) shows, 81 samples per capture evenly distributed across the sky resulted in a nearly flat distribution of
 308 sample azimuth values. The final input and output features of each sky sample used by our models are shown in Fig. 8.

309 More than 10 separate regression models were trained and tested, including: linear, Ridge (Hoerl and Kennard,
 310 1970), Lasso (Tibshirani, 1996), ElasticNet (Zou and Hastie, 2005), Lars, KNN, RandomForest (Kocev et al., 2013),
 311 ExtraTrees (Geurts et al., 2006), etc. Initially, WEKA toolkit (Hall et al., 2009) was used to discover possible candi-

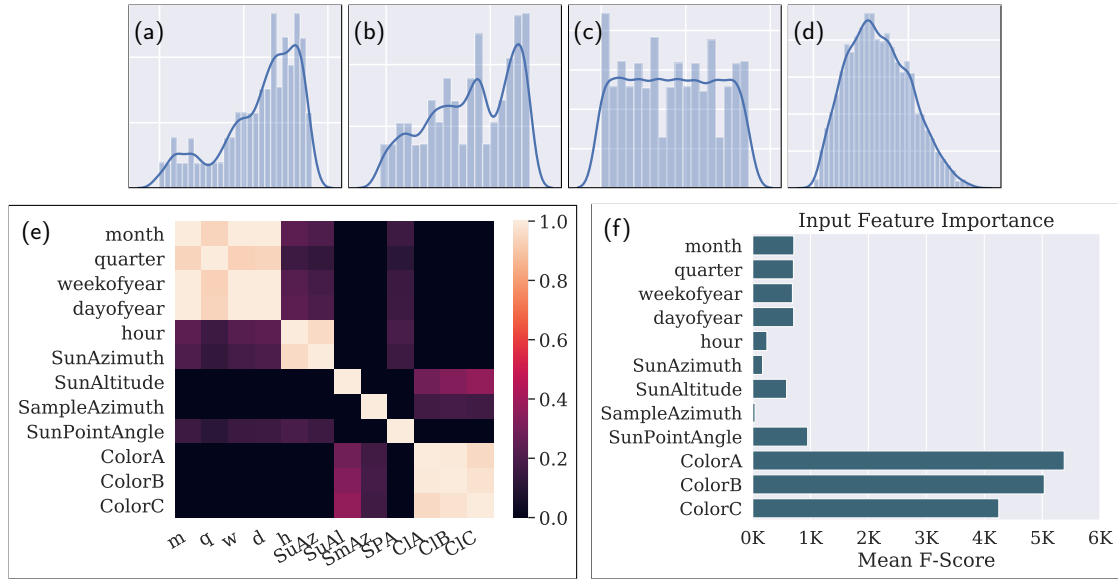


Figure 9: Plots of individual machine learning features, including histograms for (a) sun azimuth, (b) sun altitude, (c) sample azimuth, and (d) SPA. (e) shows the univariate correlation matrix of the features. Datetime components, color components, and hour of day with sun azimuth are all naturally correlated. (f) shows an estimation of importance (significance to prediction) of each feature. (d) was likely more significant because it combined the positions of both sun and sample points into a single feature. After SPA was included, sample altitude was discarded.

date models, but ultimately all machine learning models were configured and processed with scikit-learn in Python (Pedregosa et al., 2011). Initial tests of these models encouraged us to pursue the ones with promise. Many of the models forced a single decimal output value (not a vector), which didn't align with our approach; we are attempting to reconstruct a curve, or vector of radiance values per wavelength. We chose a proximity based model, like k-nearest-neighbors (KNN), and a decision tree based (ensemble) model to focus on. We also included a standard linear regressor (LNR) as a baseline, which we assumed would not perform well given the nature of the data and problem. Decision tree models implement a set of "if-then-else" rules internally for both training and prediction, and result in very large model files. We know that decision tree estimators are more prone to overfitting than any other regression model, so to further address overfitting, we used a Random Forest Regressor (RFR) specifically, which harnesses randomness to decrease variance in lieu of some bias (Kocev et al., 2013). Extra Trees Regressor (Geurts et al., 2006) introduces even more randomness and a larger trade off to combat overfitting. The final collection of tuned regression models include a linear regression (LNR), k-nearest-neighbors (KNR), random forest (RFR), and extra-trees (ETR). Although the performance of RFR and ETR are often comparable, in prior experiments we found that RFR performed significantly better on scattered cloudy skies (Del Rocco et al., 2018). For all four of our models, tuning was done mostly automatically with scikit-learn's GridSearch algorithm, though some hyperparameters were tuned manually, including the number of trees and maximum tree depth of the decision tree models.

Four separate error metrics were used to evaluate the performance of models, including: coefficient of determination score (R^2), mean bias deviation (MBD), root mean squared deviation (RMSD), and ratio of the measured and predicted radiance curves. MBD and RMSD come from Iqbal (2012):

$$RMSD = \sqrt{\frac{\sum_{i=1}^N (y_i - x_i)^2}{N}} \quad (4)$$

where N is the number of spectral radiance distributions considered, y the predicted distributions, and x the measured ground truth distributions. Recall that each distribution is a vector of radiance values between 350-1780 nm of the electromagnetic spectrum. Prior authors used MBD for single wavelength results (Cazorla et al., 2008a; Tohsing et al., 2014), but we found RMSD to be more representative of the results across a spectrum of wavelengths. The R^2 metric

335 is used during pre-holdout testing to help with model tuning, and is calculated directly from scikit-learn:

$$R^2(t, p) = 1 - \frac{\sum_{i=1}^N (t_i - p_i)^2}{\sum_{i=1}^N (t_i - \bar{t}_i)^2} , \quad (5)$$

336 where (t, p) is a (truth, prediction) pair, N is the number of radiance distributions, and $\bar{t} = \frac{1}{N} \sum_{i=1}^N t_i$. Note that this
337 metric can be negative, despite the name R^2 .

338 In addition to our dataset tool, we developed a framework of Python scripts to send datasets through our machine
339 learning pipeline of training, final testing, and plotting. The main script takes parameters such as: model type, dataset
340 of sky samples, pseudo-random number seed, number of cpu cores to use, cross-validation amount, and model-specific
341 hyperparameters such as polynomial expansion amount, maximum tree depth for decision tree pruning, etc. All source
342 code for dataset tool and pipeline is 100% cross-platform, open-source and freely available to the public through the
343 project website.²

344 4.1. High-dynamic range imagery

345 Simultaneously capturing the sun and sky with photography is difficult due to the range of illumination and intensity
346 of the sun vs. sky, as well as the temporal changes that occur. We followed the sky capture approach of Stumpfel et al.
347 (2004). We took eight to nine photographs (depending on the time of day) to capture \sim 17 stops of dynamic range.
348 Fig. 10 shows the difference in exposures captured; the top row (f/16 aperture) is best for the solar region and intensity
349 of the sun; the bottom row (f/4 aperture) is best for the indirect skylight.

350 This experiment was designed to test the effectiveness of using HDR imagery (multiple exposures) vs. a single
351 exposure of the sky. For each sky sample, we used the pixel color values from exposures 5-8 (f/4 aperture) as input
352 features for model training and prediction. Exposures 1-4 were ignored for this experiment. Although there are algo-
353 rithms to merge multiple exposures into a single image for sampling, we simply sampled each exposure separately and
354 used each sampled color as a separate input feature. Future work could include a merged color feature.

355 4.2. Color model

356 Colors are qualia for combinations of electromagnetic energy within the range of wavelengths visible to humans
357 (the visible spectrum). The human eye detects energy with the use of retinal rods and cones and the brain merges the
358 results into what we call a color (Kinney, 1958). Modeling the values of these colors is a field of research in and of
359 itself (Koenderink, 2010). And yet, we are attempting to estimate spectral radiance using color values as a primary
360 feature. This begs the research question: which color model best represents the underlying energy? Digital all-sky
361 cameras typically store measurements with trichromatic RGB color models (e.g. sRGB, Adobe RGB, ProPhotoRGB,
362 etc.), but do so mostly for historical reasons relating to technology. There are a variety of other tristimulus color models

² <https://github.com/spectralskylight>

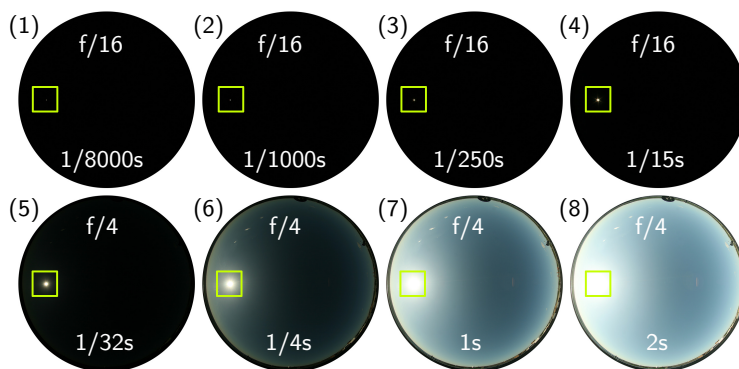


Figure 10: 8 exposures were taken to account for high dynamic range of sun + sky photography. f/4 aperture captures (5-8) were used for this work. 1 s exposure (7) was used for non-HDR experiments. Yellow squares highlight sun location.

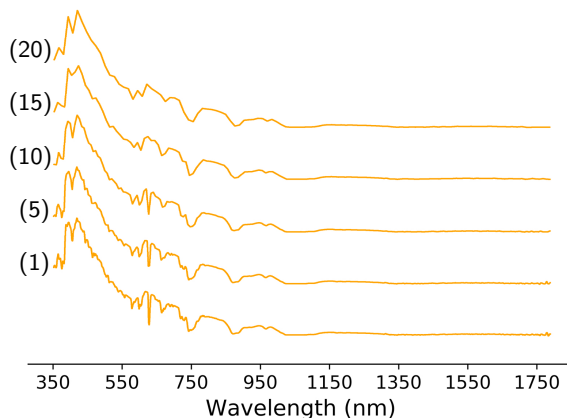


Figure 11: 05/26/2013 15:15 sample 24 (90° azimuth, 12.12° altitude) plotted at 5 different resolutions, 1, 5, 10, 15 and 20 nm, labeled accordingly. The resolution of spectral radiance distributions can be reduced depending on the downstream application.

that attempt to capture more of the color space detectable by the average human (Poynton, 1995; Stone, 2015), many of which derive from the CIE 1931 RGB and XYZ color space definitions (Wright, 1929). However, it is unclear which model is most beneficial for machine learning algorithms processing sky images.

For this experiment, we compared the overall training and predictive effectiveness of our models while only changing the color model used for each sky sample's color feature. Four separate color models were tested: sRGB (Stokes et al., 1996) (the default), HSV (Smith, 1978), HSL (Joblove and Greenberg, 1978), and LAB (Robertson et al., 1977). All other features were fixed. Because our commercial digital camera captured skies in an sRGB format, we then converted to the other color models using algorithms provided by the Python colormath module. The resulting datasets were fed through our machine learning pipeline separately.

4.3. Spectral resolution

This work is intended to be used in a real-time setting, both simulated and cyber-physical, therefore model size and processing speed is important. For applications that predict a general quantity of energy in certain parts of the spectrum, it may be reasonable to limit the resolution of spectral data used during model training and prediction. Certainly, the visual difference and area under the curve (amount of energy) between a 1 nm and 10 nm resolution curve is not significant. A spectral resolution experiment was designed to find the smallest model and dataset that still predicted with acceptable accuracy, by training and testing models using spectral resolutions of 1, 5, 10, 15 and 20 nm. Note that some pure spectral colors exist entirely within a 15 nm range, and therefore resolution should not be diminished too much if color information is important. Fig. 11 shows the visual difference of the five resolutions for a single measured radiance distribution. Depending on the downstream application, there is still plenty of useful information at lower resolutions.

This experiment was run on a Dell XPS 8920 PC with Intel 4 Core i7-7700K 4.20 GHz CPU and 16 GB of RAM. The operating system was x64-bit Microsoft Windows 10 Enterprise. All manually executable applications (i.e. ignoring operating system services) were closed at the time of the experiment. Five runs were executed per resolution size and the timings averaged.

4.4. sradmap

Downstream applications of this work may need spectral radiance estimations for the entire hemispherical sky. Ideally, our models will generalize across the space between the sky samples used for machine learning. This involves some more of interpolation or scaling of outputs between the learned skeletal space provided by our ground truth measurements, and the entire sky. If our models do not have this ability, then usage is limited to the 81 coordinates used during measurement. Obviously the higher resolution a sky scanning pattern is, the more accurate predictions will be across the sky.

To provide whole sky predictions, the same input features shown in Fig. 8 can be collected for any pixel of a sky

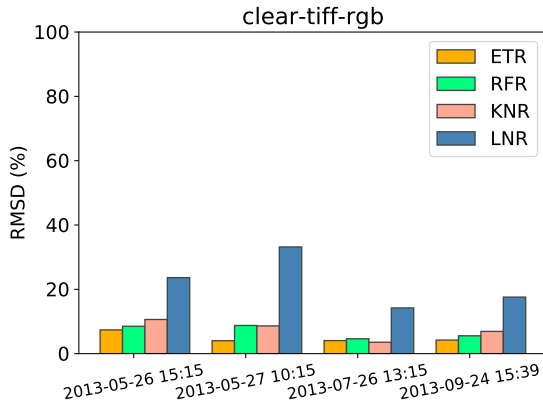


Figure 12: Model results of predicting the 81 sample point locations for each of the four holdout test skies listed in Table 1. Again, the regression models are ETR, RFR, KNR and LNR. ETR performed the best, with a total error of 4-7.5% RMSD across all 81 sample points. LNR was by far the worst performing, as expected.

image, and then fed through a single one of our models to produce a lookup file (map) with radiance predictions per pixel. We call this resulting file a spectral radiance map (sradmap). Although the primary purpose of these files is to provide a map between pixel location and spectral radiance prediction, each prediction can be summed, normalized, and plotted against a false-color map to help visualize the topology of the data.

The name sradmap is an homage to radmap by Anselmo and Lauritano (2003), a supplementary tool for the daylight simulator RADIANCE (Ward, 1994). In the building performance space, our sradmap generator can be integrated into daylight simulators, energy modelers, and parametric design tools like RADIANCE, EnergyPlus (Crawley et al., 2001), SUSTAIN (Greenberg et al., 2013), and Ladybug Tools (Roudsari et al., 2013). In the computer graphics (rendering) space, sradmaps can be sampled from renderers like Mitsuba (Jakob, 2010) or Disney's Hyperion (Burley et al., 2018), for use in scenes with natural daylighting.

5. Results

Three of the four final regression models (ETR, RFR, KNR) resulted in very high R^2 scores and acceptably low RMSD error on all holdout test skies listed in Table 1. As expected, the baseline LNR model resulted in relatively poor predictions across all test skies, with an overall error of 14-24% RMSD. By contrast, ETR resulted in 4-7.5% RMSD. For test sky 07/26/2013 13:15, three of the four models predicted within 4% RMSD. In general, the tree-based models (ETR and RFR) perform better than the nearest-neighbor model (KNN). RMSD results for all models on each test sky are shown in Fig. 12. As mentioned in section Section 4, the sample azimuth feature affected results by 1-2% RMSD, but otherwise the feature scored as least important. It is possible that the deviation in results could be within any

Fig. 13 shows a comparison of all 81 measured and ETR predicted radiance distributions, their standard deviations, and overall averaged ratio between measured and predicted on test sky 05/27/2013 10:15. The difference in standard deviations of measured and predicted is minimal, and the averaged ratio is near 1.0 for the majority of the spectrum (350-1780 nm). Note the erratic error in the ratio graph resides within an H_2O and CO_2 absorption band, where atmospheric radiance is extremely small (Lacis and Hansen, 1974), and measurements are susceptible to noise.

For the same holdout test sky (05/27/2013 10:15), Fig. 14 shows ETR prediction error across the entire hemispherical sky, and highlights the two worst spectral radiance predictions (23.63% and 21% RMSD). These two measurements occur near the sun's corona, where radiance values are traditionally higher and more erratic than the rest of a clear sky. Two other predictions selected at random are shown for comparison. A vast majority of the 81 samples are predicted to within 1% RMSD. Note that even with "high" error, predicted curves align with ground truth measurements in terms of shape. The models therefore have learned the wavelength relative intensities of the sky in accordance with capture time, sun location, etc. This is consistent with nearly all predicted results; while the magnitudes per wavelength sometimes deviate, the general shapes each predicted curve is accurate.

Although we were expecting some insight from providing multiple exposures of sky images, results seem to indicate

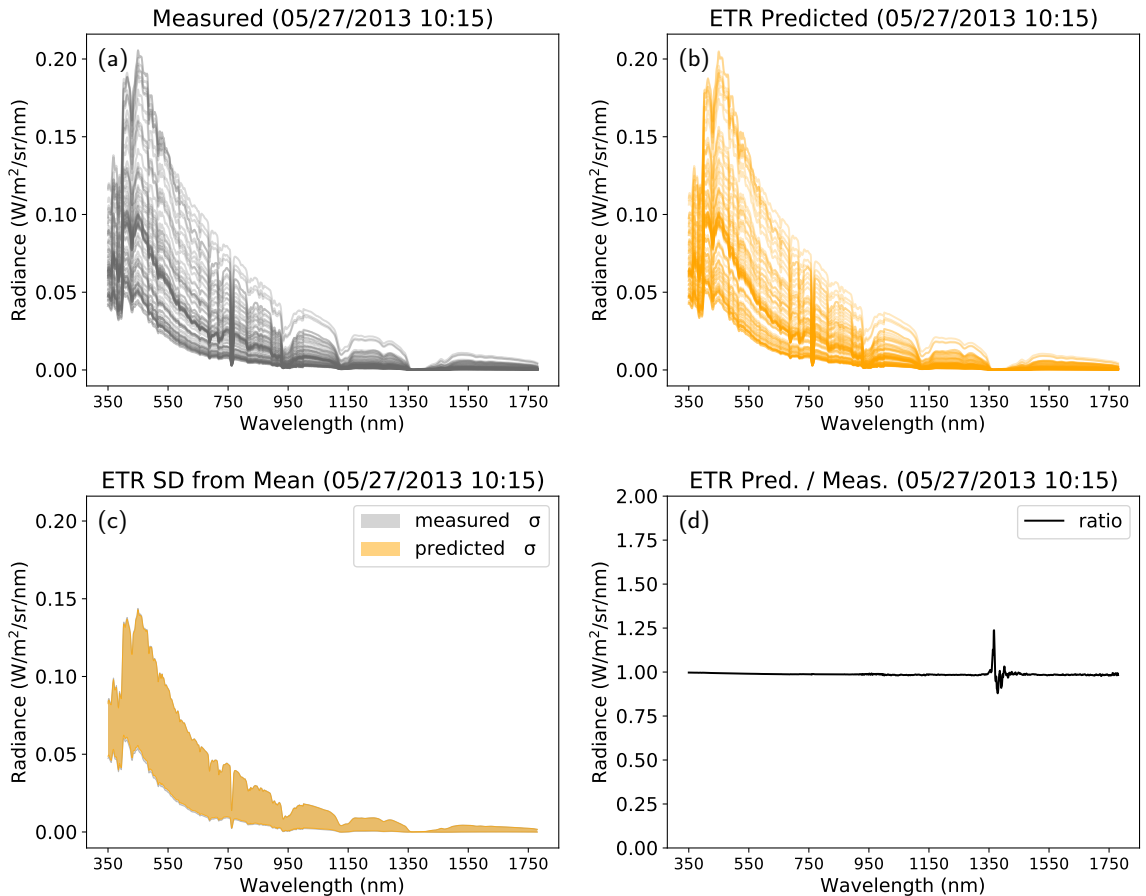


Figure 13: Whole sky results for holdout sky 05/27/2013 10:15 with ETR model. No ground truth sky samples from this capture were used for training. (a) and (b) show the 81 measured and predicted spectral radiance distributions; (c) shows the standard deviation from mean for both measured and predicted distributions; and (d) is the overall ratio between the two. Note the error in the ratio is within the absorption band near 1350 nm, where radiance is extremely small.

427 that HDR data, at least for clear skies, does not improve model prediction. All HDR runs resulted in very similar error
 428 to non-HDR runs. Similarly, differences in results between 0.25 s, 1 s, and 2 s exposures were also insignificant. We
 429 believe this may be because clear sky color changes are so “uniform” throughout the day, that multiple exposures lack
 430 significance. In other words, all provided exposures may have had the same color change trends. We suspect that HDR
 431 data will be more significant in the reconstruction of spectral radiance for scattered and overcast skies, as the color
 432 variations of clouds are less uniform across exposures.

433 Results of our color experiment (Fig. 15) seem to indicate that color model is irrelevant to our method. This implies
 434 that our method can be used with any representation of color, as the trends in color across the sky are similar regardless
 435 of format. It is unclear if using color data initially captured in an sRGB format somehow restricted the range of the
 436 other color models after conversion. In other words, would initially capturing the sky in a color model that maps to a
 437 larger color space be better?

438 The results of the spectral resolution experiment (Fig. 16) show the benefits of decreasing spectral resolution from 1
 439 to 5 nm. Model sizes (particularly the large ensemble models), as well as model training and prediction times, decrease
 440 significantly. The improvements in prediction accuracy are likely due to the radiance curve being more smooth, i.e.
 441 fewer peaks and valleys for the regression model to learn, as well as a simpler prediction problem in general, i.e. fewer
 442 outputs to predict. The size of the training dataset also decreases with reduced resolution, but that is eclipsed by the
 443 largest model sizes. Beyond 5 nm resolution, further reductions result in diminishing returns. This is an important find

Real-time spectral radiance estimation of clear skies

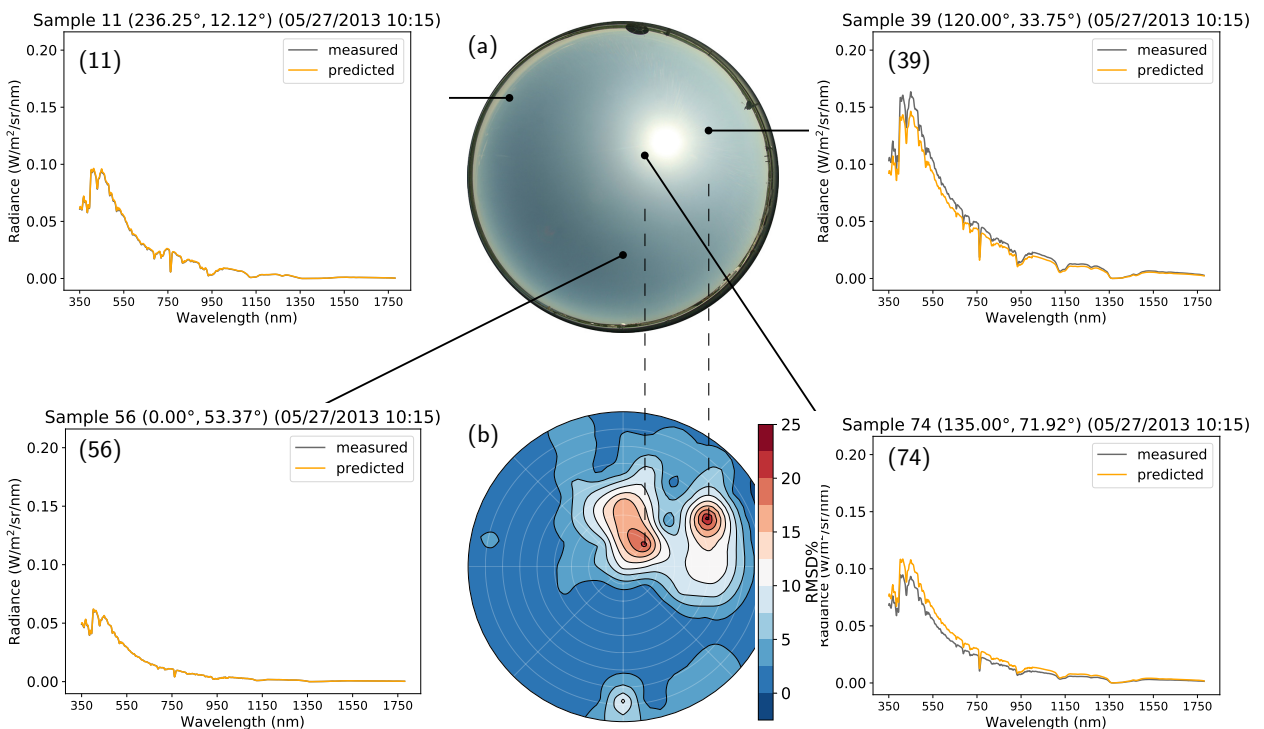


Figure 14: ETR results of four radiance predictions on holdout test sky 05/27/2013 10:15. (a) shows the camera processed JPG sky capture for convenience (the model was trained on TIFF data). (b) shows RMSD error across the entire sky. Radiance for samples (11), (56), (39) and (74) are pinpointed at their location in the sky. Samples (39) and (74) were the two worst predictions, with RMSD errors of 23.63% and 21% respectively.

for real-time applications, which may operate on limited embedded hardware.

We note here that results between the minimally processed, uncompressed TIFF sky images and traditional, camera processed, compressed JPG sky images, were roughly the same. TIFF color data resulted in slightly better results (~1%) on some skies, though this may be within the standard deviation of prediction error and machine learning random fluctuation. Since the TIFF images (~35 MB) are at least 1000% larger than the JPG images (~2.5 MB) compressed with quality level 100, and the results are similar, we recommend the use of JPG images in real-time applications of our method.

Spectral radiance files (sradmmaps) are the culminating whole sky output of our methods. They are generated by extracting features per pixel of test skies (Table 1) and feeding them through any one of our models. Linear scale false-color visualizations of ETR model predicted sradmmaps are shown in Fig. 17 and Fig. 18. Test sky images were first scaled down to a resolution of 333x333 pixels, to anticipate real-time processing speeds. sradmap generation, visualization, and logged output took ~20 s to complete on the same machine specified in Subsection 4.3; embedded hardware would likely take longer. Visualization of sradmap and logged output are not necessary for real-time applications.

6. Validation

First, no samples from our holdout test skies (Table 1), chosen at random, were used during training or preliminary testing of any model. Machine learning projects often use this method to validate a model's ability to generalize over unforeseen data. The results presented in Fig. 12, Fig. 13, and Fig. 14 show that our models have this ability. The results of our additional experiments show that our method is robust against implementation details such as image compression, exposure, and color model.

Next, the sradmmaps presented in Fig. 17 and Fig. 18 are the result of using every pixel per test sky. These maps

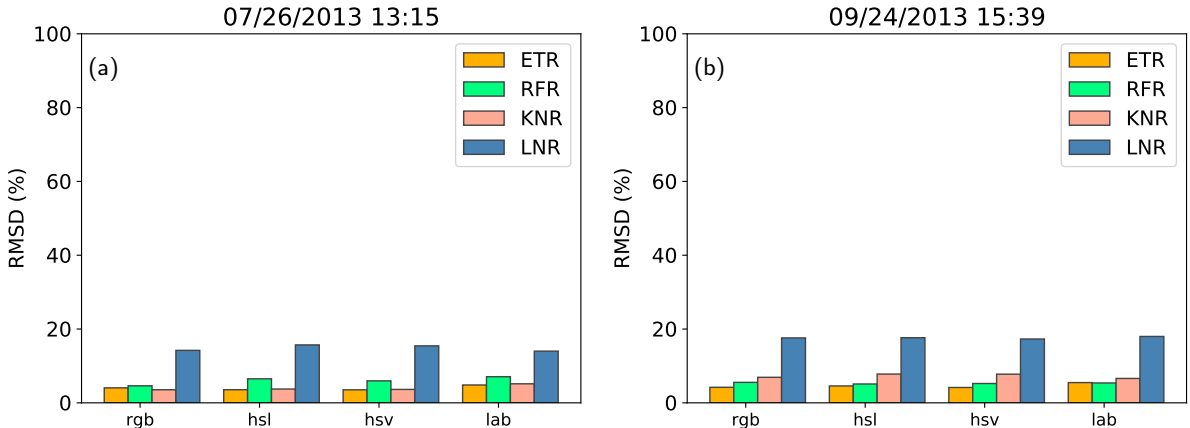


Figure 15: Sky color model made little to no difference in training and prediction results. (a) and (b) show RMSD results on 07/26/2013 13:15 and 09/24/2013 13:15 respectively.

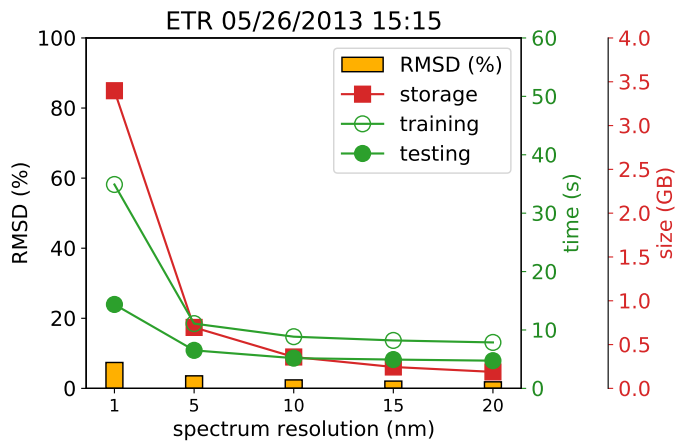


Figure 16: Limiting resolution to 5 nm drastically decreases model size, improves computation speed, and even increases prediction success, likely because the prediction problem becomes simpler with $1/5$ the number of radiance values to predict. Further reductions yield diminishing returns.

demonstrate that our models have the ability to generalize across the entire hemisphere (i.e. predict spectral radiance for every point in the sky) even when trained on a mere skeleton of samples (81 concentric 1° steradians). Note that most of the sky is unaccounted for by the skeleton, including points beyond the variance of sun and sky coordinates. sradmaps contain predictions for the entire sky.

Finally, we compare our ETR model predictions along side our ground truth measurements, with the radiance distributions computed by libRadtran (Emde et al., 2016), a popular, validated radiative transfer equation (RTE) software package that uses a variety of solvers developed in collaboration over decades and published in peer-reviewed outlets such as: the Journal of Quantitative Spectroscopy & Radiative Transfer, Atmospheric Measuring Techniques, Atmospheric Chemistry and Physics, Applied Optics, etc. MYSTIC (Buras and Mayer, 2011; Mayer, 2009; Mayer and Kylling, 2005) and DISTORT (Buras and Mayer, 2011; Dahlback and Stamnes, 1991; Stamnes et al., 1988) are the two primary comprehensive equation solvers which have been validated in multiple international model comparison studies (Emde et al., 2015; Kokhanovsky et al., 2010; Cahalan et al., 2005). Since 2005, libRadtran has been cited by hundreds of peer-reviewed publications.

libRadtran was configured the same for all four holdout test skies. In other words, no sky-specific data (atmospheric measurements, aerosol databases, parameters, or ranges) were specified per test sky - we used the default configuration.

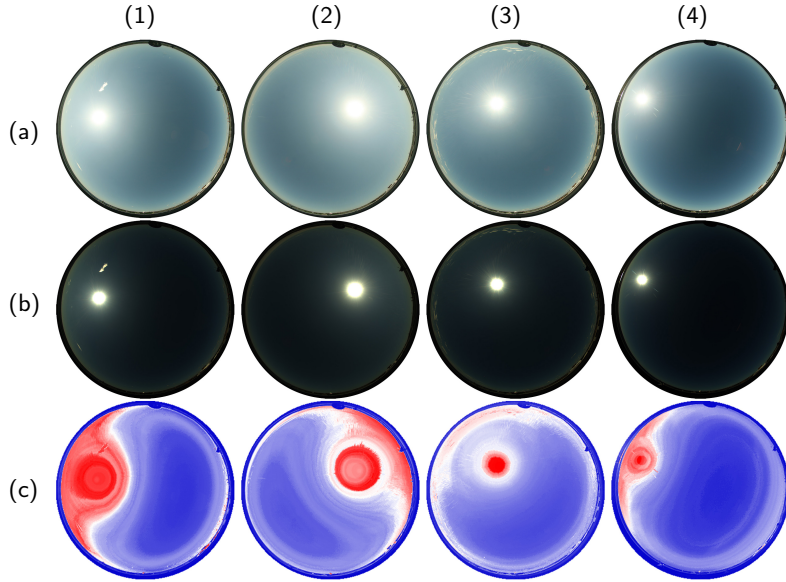


Figure 17: Columns (1-4) are the holdout test skies in Table 1, in respective order. Rows (a) and (b) show traditional, camera processed JPG and minimally processed TIFF captures, respectively. Row (c) shows the sradmap visualizations generated for skies in row (b); we use our ETR model to predict spectral radiance (350-1780 nm) for every pixel of test sky image, sum the radiance distribution, and visualize with a false-color map.

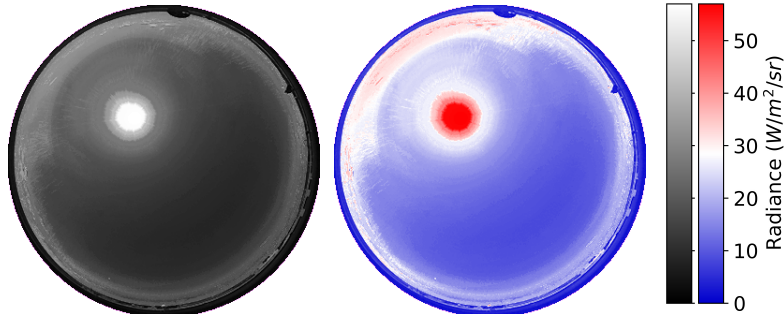


Figure 18: False-colored sradmap visualizations for holdout test sky 07/26/2013 13:15. Each pixel plotted is a summation of an entire spectral radiance distribution (350-1780 nm). There is no significance to the summation algorithm; it is simply used to visualize the data.

Fig. 19 and Fig. 20 show that libRadtran spectral radiance for three of our four holdout test skies were in alignment with both ETR model predictions and ground truth measurements. However, for test sky 07/26/2013 13:15, libRadtran deviates from both ETR predictions and ground truth measurements (Fig. 21). All tested samples for this sky show similar deviations in magnitude, but not curve shape. As mentioned, libRadtran requires accurate atmospheric data for its calculations. Because such data was not configured, and because our predictions are closer to ground truth measurements, it is possible that our ETR model learned the sky specific atmospheric conditions libRadtran needed in order to compute accurately. In particular, we note the cirrus clouds along the horizon, which might indicate ice crystals in the atmosphere, and account for deviations between data-driven predictions and physically-based model calculations.

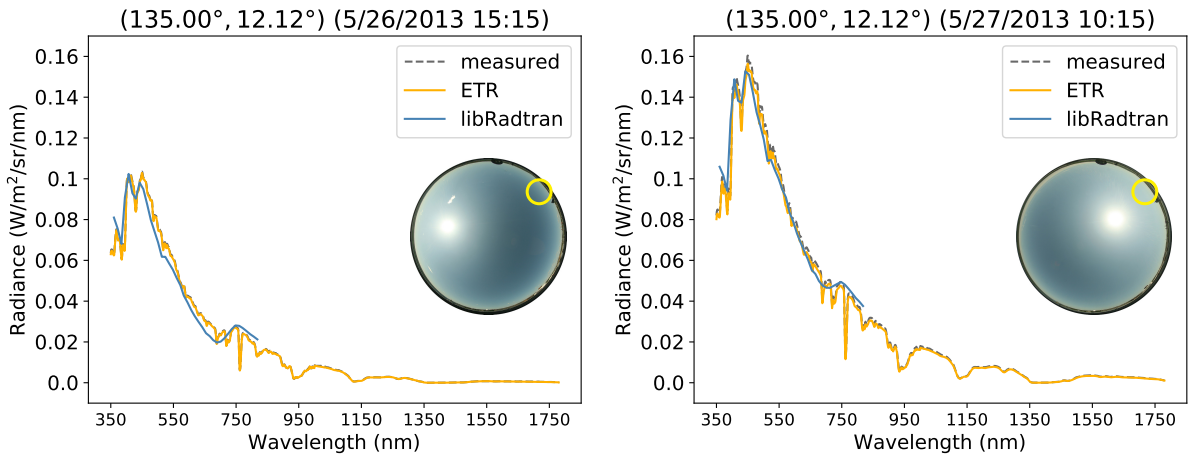


Figure 19: Spectral radiance at $(33.75^\circ$ azimuth, 12.12° altitude), circled, for two of the holdout test skies in Table 1. Spectroradiometer measurement, ETR model prediction, and libRadtran estimation plotted.

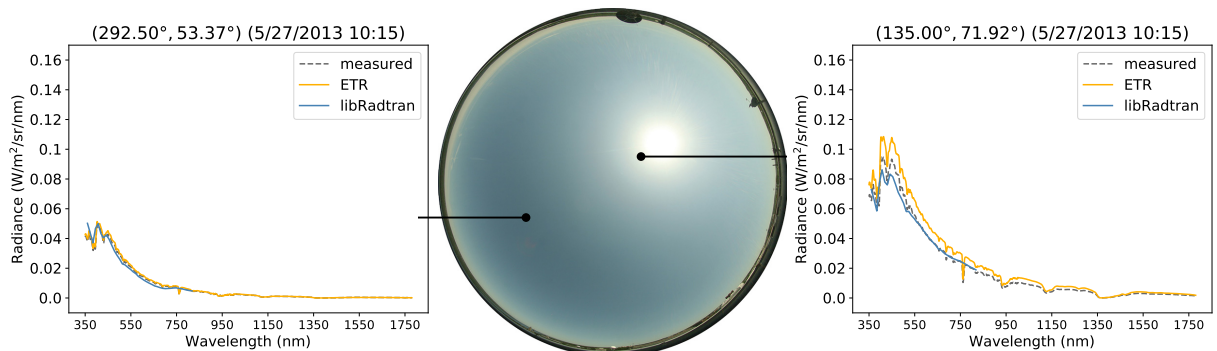


Figure 20: Spectral radiance for two sky samples of holdout test sky 05/27/2013 10:15. Spectroradiometer measurement, ETR model prediction, and libRadtran estimation plotted.

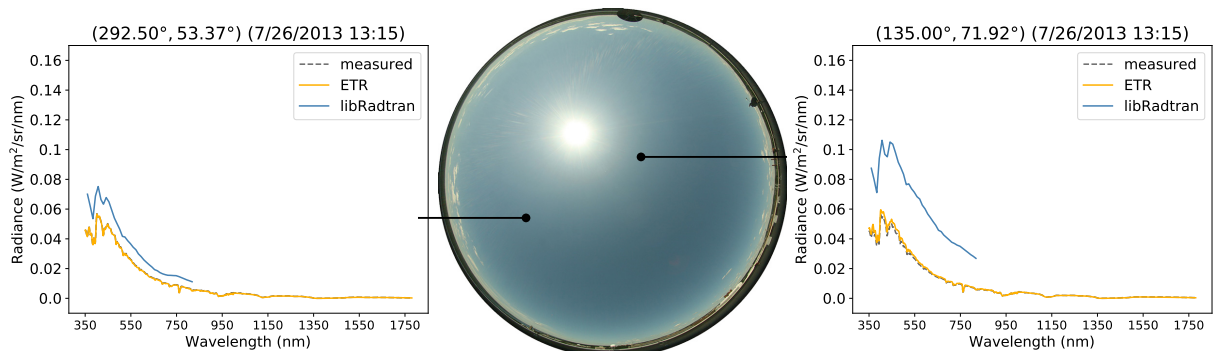


Figure 21: Spectral radiance for two sky samples of holdout test sky 07/26/2013 13:15. Spectroradiometer measurement, ETR model prediction, and libRadtran estimation plotted. libRadtran computed radiance deviates from both ETR predictions and measured ground truth data, likely because of the lack of needed atmospheric configuration data. Note the existence of cirrus clouds near the horizon.

489 7. Conclusions

490 Whole sky spectral radiance distributions are needed for accurate computations in a variety of applications, and yet
 491 they are often oversimplified. Real-time capable models are needed to estimate them to within acceptable tolerances.
 492 We presented a solution that: (1) took photographs of the entire hemispherical sky and measured the incoming radiance
 493 at various points, (2) used those measurements and modern machine learning methods to train regression models, and
 494 (3) used those models to predict atmospheric spectral radiance (350-1780 nm) at 1 nm resolution for the entire sky,
 495 given a photo of a clear sky and its capture timestamp, in ~20 s of processing time, making the solution viable for real-
 496 time applications. Our whole sky prediction error, for all four holdout test skies, none of which were used for training,
 497 was below 7.5% RMSD, and most of the predicted spectral radiance distributions were in line with libRadtran.

498 Our results show that image compression, color model, and exposure of clear sky imagery have little to no effect on
 499 our method. This implies that our solution is robust and less likely to be affected by implementation details. We also
 500 showed that our models have the ability to generalize across the hemispherical space between measured sky samples,
 501 allowing for atmospheric spectral radiance predictions for every point in a sky image.

502 Our trained models can be used as-is, with similarly exposed and oriented sky photos. And our methods can be
 503 reproduced to train models using new datasets. Various sky scanning systems exist which can be employed to provide
 504 regional training data. Existing correlated sky imagery and spectral radiance datasets from around the world can (and
 505 should) be used with our method. Once normalized, such comprehensive datasets could lead to even more robust
 506 models (e.g. more variations of sky turbidity). As mentioned, aerosol data can also be included as training and pre-
 507 diction features, supplied from local building sensors, GOES satellite measurements, and/or triangulated atmospheric
 508 measuring station data. Site location coordinates and/or elevation could also be investigated as input features when
 509 using multi-site data. More spectral radiance measurements within the circumsolar region would also likely improve
 510 accuracy (clear or cloudy sky), as the bulk of the energy is accounted for within that region of the sky. All research in
 511 this area could benefit by a scanning pattern that accounts for this.

512 Although many downstream applications of our research are possible, one immediately viable option is a building
 513 monitoring system equipped with all-sky camera that adjusts smart glazing and kinetic facades in response to spectral
 514 radiance across the entire non-occluded sky. Such a system would automatically harness (or attenuate) light and heat
 515 with more fine-grain control and accuracy than one that operates on a single downwelling measurement, and would be
 516 much more affordable and efficient than a live, continuously operating sky scanning system. As mentioned, various
 517 procedural processes can be applied to distinguish clear, scattered, and overcast skies, so that pixels and image regions
 518 can be passed to appropriate models for spectral radiance prediction. Cloud detection research regularly separates
 519 clear from cloudy portions of skies. We hope our research motivates the building performance community to further
 520 refine such a system. We also hope that the graphics (rendering) community notices the useful of our sradmap tool.
 521 The predicted spectral radiance distributions can and should be used in spectral renderers (the future of rendering) to
 522 provide the most accurate natural day-lighting scenes.

523 Further work will focus on scattered cloudy skies. Scattered skies account for the bulk of our publicly available
 524 dataset (63%), and in general is more complicated to model. Although our preliminary results showed that an RFR re-
 525 gression model performed moderately well on 3 our 4 test skies (Del Rocco et al., 2018), we feel that more progress can
 526 be made with more complex machine-learning techniques, such as neural networks. Simply throwing our entire dataset
 527 (clear, scattered, and overcast data) at a neural architecture search (NAS) deep learning neural network infrastructure,
 528 we achieved an 83% R^2 score, suggesting there is potential for a unified machine learned model. More investigation
 529 is needed to find the right network configuration to handle this problem. We also believe that HDR data will have
 530 more of an impact on cloudy versus clear skies, because the color gradients are not nearly as uniform. Additional work
 531 should include improving our Gaussian weighted color sampling with rectangular (as opposed to square) convolution
 532 kernels, to capture the projected solid angle area (ellipse) precisely.

533 Portions of this work were presented at SPIE Optics and Photonics for Information Processing XII (Del Rocco
 534 et al., 2018).

535 References

- 536 Anselmo, F., Lauritano, A., 2003. Evaluation of the solar energy potential in urban settings by irradiation map production, in: 2nd International
 537 Radiance Workshop, Radiance Community, Berkeley, California. pp. 1–1. <https://www.radiance-online.org/community/workshops/>.
- 538 Arking, A., Childs, J.D., 1985. Retrieval of cloud cover parameters from multispectral satellite images. Journal of Climate and Applied Meteorology
 539 24, 322–333.

- Berk, A., Conforti, P., Kennett, R., Perkins, T., Hawes, F., Van Den Bosch, J., 2014. MODTRAN 6: A major upgrade of the MODTRAN radiative transfer code, in: 2014 6th Workshop on Hyperspectral Image and Signal Processing: Evolution in Remote Sensing (WHISPERS), IEEE. pp. 1–4. <https://doi.org/10.1109/WHISPERS.2014.8077573>.
- Bourke, P., 2016. Lens correction and distortion. Professional web site: <http://paulbourke.net/dome/fisheyecorrect>.
- Bruneton, E., 2016. A qualitative and quantitative evaluation of 8 clear sky models. *IEEE transactions on visualization and computer graphics* 23, 2641–2655. <https://doi.org/10.1109/TVCG.2016.2622272>.
- Buras, R., Mayer, B., 2011. Efficient unbiased variance reduction techniques for monte carlo simulations of radiative transfer in cloudy atmospheres: The solution. *Journal of quantitative spectroscopy and radiative transfer* 112, 434–447.
- Burley, B., Adler, D., Chiang, M.J.Y., Driskill, H., Habel, R., Kelly, P., Kutz, P., Li, Y.K., Teece, D., 2018. The design and evolution of Disney's Hyperion renderer. *ACM Transactions on Graphics (TOG)* 37, 33. <https://doi.org/10.1145/3182159>.
- Butler, D., 2008. Architects of a low-energy future: low-and zero-energy buildings could have a huge impact on energy use and carbon emissions. we have the technologies, but if they are to mitigate climate change, green-building design must hit the mass market. *Nature* 452, 520–524.
- Cahalan, R.F., Oreopoulos, L., Marshak, A., Evans, K.F., Davis, A.B., Pincus, R., Yetzer, K.H., Mayer, B., Davies, R., Ackerman, T.P., et al., 2005. The i3rc: Bringing together the most advanced radiative transfer tools for cloudy atmospheres. *Bulletin of the American Meteorological Society* 86, 1275–1294.
- Cazorla, A., Olmo, F., Alados-Arboledas, L., 2008a. Using a sky imager for aerosol characterization. *Atmospheric Environment* 42, 2739–2745.
- Cazorla, A., Olmo, F.J., Alados-Arboledas, L., 2008b. Development of a sky imager for cloud cover assessment. *JOSA A* 25, 29–39.
- Chandrasekhar, S., 1950. Radiative Transfer. Oxford University Press.
- Chandrasekhar, S., 2013. Radiative transfer. Courier Corporation.
- Chauvin, R., Nou, J., Thil, S., Grieu, S., 2015. Modelling the clear-sky intensity distribution using a sky imager. *Solar Energy* 119, 1–17. <https://doi.org/10.1016/j.solener.2015.06.026>.
- Chen, Y., Alspaugh, S., Katz, R., 2012. Interactive analytical processing in big data systems: A cross-industry study of mapreduce workloads. arXiv preprint arXiv:1208.4174 .
- Chinchor, N., 1992. The statistical significance of the muc-4 results, in: Proceedings of the 4th conference on Message understanding, Association for Computational Linguistics. pp. 30–50.
- Cooper, W.S., 1973. On selecting a measure of retrieval effectiveness. *Journal of the American Society for Information Science* 24, 87–100.
- Cordero, R.R., Damiani, A., Ferrer, J., Rayas, J., Jorquer, J., Tobar, M., Labbe, F., Laroze, D., 2013. Downwelling and upwelling radiance distributions sampled under cloudless conditions in Antarctica. *Applied Optics* 52, 6287. URL: <https://www.osapublishing.org/abstract.cfm?URI=ao-52-25-6287>, doi:10.1364/AO.52.006287.
- Cornette, W.M., Shanks, J.G., 1992. Physically reasonable analytic expression for the single-scattering phase function. *Applied optics* 31, 3152–3160. <https://doi.org/10.1364/AO.31.003152>.
- Crawley, D.B., Lawrie, L.K., Winkelmann, F.C., Buhl, W.F., Huang, Y.J., Pedersen, C.O., Strand, R.K., Liesen, R.J., Fisher, D.E., Witte, M.J., et al., 2001. Energyplus: creating a new-generation building energy simulation program. *Energy and buildings* 33, 319–331. [https://doi.org/10.1016/S0378-7788\(00\)00114-6](https://doi.org/10.1016/S0378-7788(00)00114-6).
- Dahlback, A., Stamnes, K., 1991. A new spherical model for computing the radiation field available for photolysis and heating at twilight. *Planetary and Space Science* 39, 671–683.
- Del Rocco, J., Patterson, C.B., Dhrif, H., Kider, J.T., 2018. Learning and estimating whole sky visible, vnir, swir radiance distributions from a commercial camera, in: Optics and Photonics for Information Processing XII, SPIE. p. 107510F. <https://doi.org/10.1117/12.2321295>.
- Eltbaakh, Y.A., Ruslan, M.H., Alghoul, M., Othman, M.Y., Sopian, K., Razikov, T., 2012. Solar attenuation by aerosols: An overview. *Renewable and Sustainable Energy Reviews* 16, 4264–4276.
- Emde, C., Barlakas, V., Cornet, C., Evans, F., Korkin, S., Ota, Y., Labonne, L.C., Lyapustin, A., Macke, A., Mayer, B., et al., 2015. Iprt polarized radiative transfer model intercomparison project-phase a. *Journal of Quantitative Spectroscopy and Radiative Transfer* 164, 8–36.
- Emde, C., Buras-Schnell, R., Kylling, A., Mayer, B., Gasteiger, J., Hamann, U., Kylling, J., Richter, B., Pause, C., Dowling, T., et al., 2016. The libRadtran software package for radiative transfer calculations (version 2.0.1). *Geoscientific Model Development* , 1647–1672.
- Fisher, R., Perkins, S., Walker, A., Wolfart, E., 1996. Hypermedia image processing reference. John Wiley & Sons Ltd. <https://www.worldcat.org/title/hypermedia-image-processing-reference/oclc/43115444>.
- Gandomi, A., Haider, M., 2015. Beyond the hype: Big data concepts, methods, and analytics. *International journal of information management* 35, 137–144.
- Geurts, P., Ernst, D., Wehenkel, L., 2006. Extremely randomized trees. *Machine learning* 63, 3–42.
- Greenberg, D., Pratt, K., Hencey, B., Jones, N., Schumann, L., Dobbs, J., Dong, Z., Bosworth, D., Walter, B., 2013. Sustain: An experimental test bed for building energy simulation. *Energy and Buildings* 58, 44–57. <https://doi.org/10.1016/j.enbuild.2012.11.026>.
- Guemard, C., et al., 1995. SMARTS2 A: simple model of the atmospheric radiative transfer of sunshine: algorithms and performance assessment. Florida Solar Energy Center (FSEC) Cocoa, FL. <https://www.nrel.gov/grid/solar-resource/smarts.html>.
- Haber, J., Magnor, M., Seidel, H.P., 2005. Physically-based simulation of twilight phenomena. *ACM Transactions on Graphics (TOG)* 24, 1353–1373. <https://doi.org/10.1145/1095878.1095884>.
- Hall, M., Frank, E., Holmes, G., Pfahringer, B., Reutemann, P., Witten, I.H., 2009. The weka data mining software: an update. *ACM SIGKDD explorations newsletter* 11, 10–18. <https://doi.org/10.1145/1656274.1656278>.
- Hensen, J.L., Lamberts, R., 2012. Building performance simulation for design and operation. Routledge.
- Henyey, L.G., Greenstein, J.L., 1941. Diffuse radiation in the galaxy. *The Astrophysical Journal* 93, 70–83.
- Hess, M., Koepke, P., Schult, I., 1998. Optical properties of aerosols and clouds: The software package opac. *Bulletin of the American meteorological society* 79, 831–844.
- Hoerl, A.E., Kennard, R.W., 1970. Ridge regression: Biased estimation for nonorthogonal problems. *Technometrics* 12, 55–67.
- Holben, B.N., Eck, T.F., Slutsker, I., Tanre, D., Buis, J., Setzer, A., Vermote, E., Reagan, J.A., Kaufman, Y., Nakajima, T., et al., 1998. Aeronet—a

- federated instrument network and data archive for aerosol characterization. *Remote sensing of environment* 66, 1–16.
- Hosek, L., Wilkie, A., 2012. An analytic model for full spectral sky-dome radiance. *ACM Transactions on Graphics (TOG)* 31, 95. <https://doi.org/10.1145/2185520.2185591>.
- Igawa, N., Nakamura, H., 2001. All sky model as a standard sky for the simulation of daylit environment. *Building and Environment* 36, 763–770. [https://doi.org/10.1016/S0360-1323\(00\)00062-7](https://doi.org/10.1016/S0360-1323(00)00062-7).
- Iqbal, M., 2012. An introduction to solar radiation. Elsevier.
- Jakica, N., 2017. State-of-the-art review of solar design tools and methods for assessing daylighting and solar potential for building-integrated photovoltaics. *Renewable and Sustainable Energy Reviews* .
- Jakob, W., 2010. Mitsuba renderer. <Http://www.mitsuba-renderer.org>.
- Jarosz, W., 2008. Efficient Monte Carlo methods for light transport in scattering media. Citeseer.
- Joblove, G.H., Greenberg, D., 1978. Color spaces for computer graphics, in: *ACM SIGGRAPH Computer Graphics*, ACM. pp. 20–25. <https://doi.org/10.1145/965139.807362>.
- Kajiya, J.T., 1986. The rendering equation, in: *ACM SIGGRAPH computer graphics*, ACM. pp. 143–150. <https://doi.org/10.1145/15886.15902>.
- Kider, J.T., Knowlton, D., Newlin, J., Li, Y.K., Greenberg, D.P., 2014. A framework for the experimental comparison of solar and skydome illumination. *ACM Transactions on Graphics (TOG)* 33, 180. <https://doi.org/10.1145/2661229.2661259>.
- Kinney, J.A.S., 1958. Comparison of scotopic, mesopic, and photopic spectral sensitivity curves. *JOSA* 48, 185–190. <https://doi.org/10.1364/JOSA.48.000185>.
- Kittler, R., 1994. Some qualities of scattering functions defining sky radiance distributions. *Solar Energy* 53, 511–516. [https://doi.org/10.1016/0038-092X\(94\)90131-K](https://doi.org/10.1016/0038-092X(94)90131-K).
- Kocev, D., Vens, C., Struyf, J., Džeroski, S., 2013. Tree ensembles for predicting structured outputs. *Pattern Recognition* 46, 817–833.
- Kocifaj, M., 2009. Sky luminance/radiance model with multiple scattering effect. *Solar Energy* 83, 1914–1922. <https://doi.org/10.1016/j.solener.2009.07.004>.
- Kocifaj, M., 2012. Angular distribution of scattered radiation under broken cloud arrays: an approximation of successive orders of scattering. *Solar Energy* 86, 3575–3586. <https://doi.org/10.1016/j.solener.2012.06.022>.
- Kocifaj, M., 2015. Unified model of radiance patterns under arbitrary sky conditions. *Solar Energy* 115, 40–51. <http://linkinghub.elsevier.com/retrieve/pii/S0038092X15000894>.
- Koenderink, J.J., 2010. *Color for the Sciences*. The MIT Press.
- Kohavi, R., et al., 1995. A study of cross-validation and bootstrap for accuracy estimation and model selection, in: *Ijcai*, Montreal, Canada. pp. 1137–1145.
- Kokhanovsky, A.A., Budak, V.P., Cornet, C., Duan, M., Emde, C., Katsev, I.L., Klyukov, D.A., Korkin, S.V., C-Labonnote, L., Mayer, B., et al., 2010. Benchmark results in vector atmospheric radiative transfer. *Journal of Quantitative Spectroscopy and Radiative Transfer* 111, 1931–1946.
- Kylling, A., Stammes, K., Tsay, S.C., 1995. A reliable and efficient two-stream algorithm for spherical radiative transfer: Documentation of accuracy in realistic layered media. *Journal of Atmospheric Chemistry* 21, 115–150.
- Lacis, A.A., Hansen, J., 1974. A parameterization for the absorption of solar radiation in the earth's atmosphere. *Journal of the atmospheric sciences* 31, 118–133. [https://doi.org/10.1175/1520-0469\(1974\)031%3C0118:APFTA0%3E2.0.CO;2](https://doi.org/10.1175/1520-0469(1974)031%3C0118:APFTA0%3E2.0.CO;2).
- Laney, D., 2001. 3d data management: Controlling data volume, velocity and variety. *META group research note* 6, 1.
- Lee Jr, R.L., 2008. Measuring overcast colors with all-sky imaging. *Applied optics* 47, H106–H115.
- Li, Q., Lu, W., Yang, J., 2011. A hybrid thresholding algorithm for cloud detection on ground-based color images. *Journal of atmospheric and oceanic technology* 28, 1286–1296.
- LibRaw, 2018. libraw, raw image decoder. <https://www.libraw.org>.
- Littlefair, P.J., 1981. The luminance distribution of an average sky. *Lighting Research & Technology* 13, 192–198. <https://doi.org/10.1177/09603271801300402>.
- López-Álvarez, M.A., Hernández-Andrés, J., Romero, J., Olmo, F.J., Cazorla, A., Alados-Arboledas, L., 2008. Using a trichromatic CCD camera for spectral skylight estimation. *Applied optics* 47, H31–H38. URL: <https://www.osapublishing.org/abstract.cfm?uri=ao-47-34-h31>.
- Macskassy, S.A., Hirsh, H., 2003. Adding numbers to text classification, in: *Proceedings of the twelfth international conference on Information and knowledge management*, ACM. pp. 240–246. <https://doi.org/10.1145/956863.956910>.
- Malthus, T., MacLellan, C., 2010. High performance fore optic accessories and tools for reflectance and radiometric measurements with the ASD FR3 spectroradiometer, in: *ESA Hyperspectral Workshop 2010 “From Chris/Proba to PRISMA and EnMAP and beyond”*, European Space Agency. p. EP101432. <http://hdl.handle.net/102.100.100/108223>.
- Mayer, B., 2009. Radiative transfer in the cloudy atmosphere, in: *EPJ Web of Conferences*, EDP Sciences. pp. 75–99.
- Mayer, B., Kylling, A., 2005. The libRadtran software package for radiative transfer calculations. *Atmospheric Chemistry and Physics* 5, 1855–1877.
- Mazria, E., Kershner, K., 2008. Meeting the 2030 challenge through building codes. *Architecture 2030*.
- Mie, G., 1908. Beiträge zur optik trüber medien, speziell kolloidalen metallösungen. *Annalen der physik* 330, 377–445.
- Mishchenko, M.I., Travis, L.D., Lacis, A.A., 2002. Scattering, absorption, and emission of light by small particles. Cambridge university press.
- Nakamura, H., Oki, M., Hayashi, Y., 1985. A study on the estimation of the relative frequency of occurrences of the clear sky, the intermediate sky and the overcast sky in japan. *Journal of Light & Visual Environment* 9, 2_22–2_31. https://doi.org/10.2150/jlve.9.2_22.
- Nishita, T., Dobashi, Y., Nakamae, E., 1996. Display of clouds taking into account multiple anisotropic scattering and sky light, in: *Proceedings of the 23rd annual conference on Computer graphics and interactive techniques*, ACM. pp. 379–386. <https://doi.org/10.1145/237170.237277>.
- Nishita, T., Sirai, T., Nakamae, E., Tadamura, K., 1993. Display of the earth taking into account atmospheric scattering, in: *SIGGRAPH*, p. 175. <https://doi.org/10.1145/166117.166140>.
- Nou, J., Chauvin, R., Eynard, J., Thil, S., Grieu, S., 2018. Towards the intrahour forecasting of direct normal irradiance using sky-imaging data.

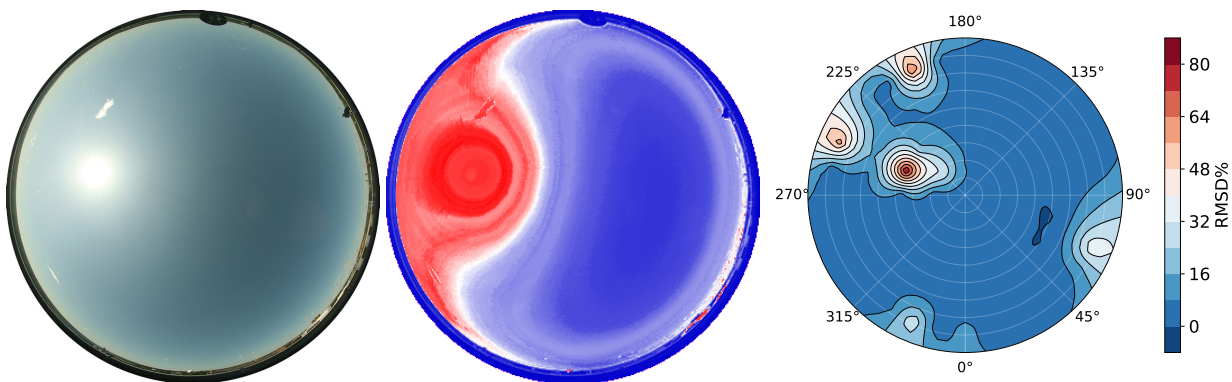
- 666 Heliyon 4, e00598. <https://doi.org/10.1016/j.heliyon.2018.e00598>.
- 667 Office Of The Federal Coordinator For Meteorological Services And Supporting Research, 2017. Chapter 9: Sky Condition, in: Federal Meteo-
668 rological Handbook No. 1: Surface Weather Observations and Reports. fcm-h1-2017 ed.. National Oceanic and Atmospheric Administration,
669 Washington, D.C., pp. 45–50. URL: https://www.ofcm.gov/publications/fmh/FMH1/FMH1_2017.pdf.
- 670 Parker, J.R., 2010. Algorithms for image processing and computer vision. John Wiley & Sons. <https://www.worldcat.org/title/algorithms-for-image-processing-and-computer-vision/oclc/813666888>.
- 671 Pedregosa, F., Varoquaux, G., Gramfort, A., Michel, V., Thirion, B., Grisel, O., Blondel, M., Prettenhofer, P., Weiss, R., Dubourg, V., et al., 2011.
672 Scikit-learn: Machine learning in python. Journal of machine learning research 12, 2825–2830.
- 673 Perez, R., Seals, R., Michalsky, J., 1993. All-weather model for sky luminance distribution—preliminary configuration and validation. Solar energy
674 50, 235–245. [https://doi.org/10.1016/0038-092X\(93\)90017-I](https://doi.org/10.1016/0038-092X(93)90017-I).
- 675 Picard, R.R., Cook, R.D., 1984. Cross-validation of regression models. Journal of the American Statistical Association 79, 575–583. <https://doi.org/10.1080/01621459.1984.10478083>.
- 676 Pokrowski, G., 1929. Über einen scheinbaren mie-effekt und seine mögliche rolle in der atmosphärenoptik. Zeitschrift für Physik 53, 67–71.
- 677 Poynton, C.A., 1995. A guided tour of colour space, in: New Foundation for Video Technology: The SMPTE Advanced Television and Electronic
678 Imaging Conference, SMPTE. pp. 167–180. <https://doi.org/10.5594/M00840>.
- 679 Preetham, A., Shirley, P., Smits, B., 1999. A practical analytic model for daylight, in: Proceedings of the 26th Annual Conference on Computer
680 Graphics and Interactive Techniques, ACM. ACM Press/Addison-Wesley Publishing Co.. pp. 91–100. <https://doi.org/10.1145/311535.311545>.
- 681 Reda, I., Andreas, A., 2004. Solar position algorithm for solar radiation applications. Solar energy 76, 577–589. <https://doi.org/10.1016/j.solener.2003.12.003>.
- 682 Ricchiazzi, P., Yang, S., Gautier, C., Sowle, D., 1998. Sbdart: A research and teaching software tool for plane-parallel radiative transfer in the earth's
683 atmosphere. Bulletin of the American Meteorological Society 79, 2101–2114. [https://doi.org/10.1175/1520-0477\(1998\)079<2101:SARATS>2.0.CO;2](https://doi.org/10.1175/1520-0477(1998)079<2101:SARATS>2.0.CO;2).
- 684 Riechert, M., 2018. rawpy (0.13.1), RAW image processing for Python. <https://pypi.org/project/rawpy>.
- 685 Robertson, A.R., et al., 1977. The CIE 1976 color-difference formulae. Color Research & Application 2, 7–11. <https://doi.org/10.1002/j.1520-6378.1977.tb00104.x>.
- 686 Roudsari, M.S., Pak, M., Smith, A., et al., 2013. Ladybug: A parametric environmental plugin for Grasshopper to help designers create an
687 environmentally-conscious design, in: Proceedings of the 13th international IBPSA conference held in Lyon, France Aug, pp. 3128–3135.
688 https://www.ibpsa.org/proceedings/bs2013/p_2499.pdf.
- 689 Sagiroglu, S., Sinanc, D., 2013. Big data: A review, in: 2013 international conference on collaboration technologies and systems (CTS), IEEE. pp.
690 42–47.
- 691 Saito, M., Iwabuchi, H., 2016. Cloud Discrimination from Sky Images Using a Clear-Sky Index. Journal of Atmospheric and Oceanic Technology
692 33, 1583–1595. URL: <http://journals.ametsoc.org/doi/10.1175/JTECH-D-15-0204.1>, doi:10.1175/JTECH-D-15-0204.1.
- 693 Saito, M., Iwabuchi, H., Murata, I., 2016. Estimation of spectral distribution of sky radiance using a commercial digital camera. Applied Optics
694 55, 415. <https://doi.org/10.1364/AO.55.000415>.
- 695 Sasaki, Y., 2007. The truth oh the f-measure. Technical Report, Version: 26th .
- 696 Satylmys, P., Bashford-Rogers, T., Chalmers, A., Debattista, K., 2016. A machine-learning-driven sky model. IEEE computer graphics and
697 applications 37, 80–91. <https://doi.org/10.1109/MCG.2016.67>.
- 698 Sigernes, F., Holmes, J.M., Dyrland, M., Lorentzen, D.A., Svenøe, T., Heia, K., Aso, T., Chernouss, S., Deehr, C.S., 2008. Sensitivity calibration
699 of digital colour cameras for auroral imaging. Optics express 16, 15623–15632.
- 700 Smith, A.R., 1978. Color gamut transform pairs. ACM SIGGRAPH Computer Graphics 12, 12–19. <https://doi.org/10.1145/965139.807361>.
- 701 Smith, C.J., Forster, P.M., Crook, R., 2016. An all-sky radiative transfer method to predict optimal tilt and azimuth angle of a solar collector. Solar
702 Energy 123, 88–101.
- 703 Stammes, K., Tsay, S.C., Wiscombe, W., Jayaweera, K., 1988. Numerically stable algorithm for discrete-ordinate-method radiative transfer in
704 multiple scattering and emitting layered media. Applied optics 27, 2502–2509.
- 705 Stokes, M., Anderson, M., Chandrasekar, S., Motta, R., 1996. A standard default color space for the internet-sRGB. Microsoft and Hewlett-Packard
706 Joint Report <https://www.w3.org/Graphics/Color/sRGB>.
- 707 Stone, E., 2015. Completely painless programmer's guide to XYZ, RGB, ICC, xyY, and TRCs. Personal website <https://ninedegreesbelow.com/photography/xyz-rgb.html>.
- 708 Strutt, J.W., 1871. On the light from the sky, its polarization and colour. The London, Edinburgh, and Dublin Philosophical Magazine and Journal
709 of Science 41, 107–120.
- 710 Stumpfel, J., Tchou, C., Jones, A., Hawkins, T., Wenger, A., Debevec, P., 2004. Direct hdr capture of the sun and sky, in: Proceedings of the 3rd
711 International Conference on Computer Graphics, Virtual Reality, Visualisation and Interaction in Africa, ACM. pp. 145–149. <http://doi.acm.org/10.1145/1029949.1029977>.
- 712 Tibshirani, R., 1996. Regression shrinkage and selection via the lasso. Journal of the Royal Statistical Society. Series B (Methodological) , 267–288.
- 713 Tohsing, K., Schrempf, M., Riechelmann, S., Seckmeyer, G., 2014. Validation of spectral sky radiance derived from all-sky camera images-a case
714 study. Atmospheric Measurement Techniques 7 (2014), Nr. 7. <https://doi.org/10.15488/5>.
- 715 Van Rijsbergen, C., 1979. Information Retrieval. Butterworths.
- 716 Vermote, E., Tanré, D., Deuzé, J., Herman, M., Morcrette, J., Kotchenova, S., 2006. Second simulation of a satellite signal in the solar spectrum-
717 vector (6SV). 6S User Guide Version 3, 1–55.
- 718 Ward, G.J., 1994. The RADIANCE lighting simulation and rendering system, in: Proceedings of the 21st annual conference on Computer graphics
719 and interactive techniques, ACM. pp. 459–472. <https://doi.org/10.1145/192161.192286>.

- 729 Wright, W.D., 1929. A re-determination of the trichromatic coefficients of the spectral colours. *Transactions of the Optical Society* 30, 141.
730 <https://doi.org/10.1088/1475-4878/30/4/301>.
- 731 Yamashita, M., Yoshimura, M., Nakashizuka, T., 2004. Cloud cover estimation using multitemporal hemisphere imageries. *International Archives
732 of Photogrammetry Remote Sensing and Spatial Information Sciences* 35, 826–829.
- 733 Yao, W., Li, Z., Zhao, Q., Lu, Y., Lu, R., 2015. A new anisotropic diffuse radiation model. *Energy Conversion and Management* 95, 304–313.
734 <https://doi.org/10.1016/j.enconman.2015.01.016>.
- 735 Yu, C.H., 1977. Exploratory data analysis. *Methods* 2, 131–160. <https://dx.doi.org/10.1093/obo/9780199828340-0200>.
- 736 Zotti, G., Wilkie, A., Purgathofer, W., 2007. A critical review of the preetham skylight model, in: *WSCG '2007: Short Communications Proceedings*,
737 Václav Skala-UNION Agency. pp. 23–30. <http://hdl.handle.net/11025/11160>.
- 738 Zou, H., Hastie, T., 2005. Regularization and variable selection via the elastic net. *Journal of the Royal Statistical Society: Series B (Statistical
739 Methodology)* 67, 301–320.
- 740

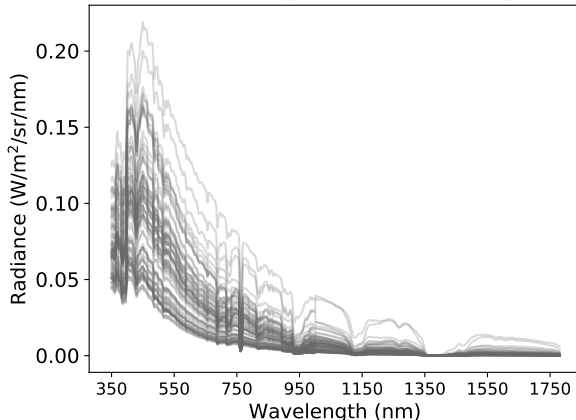
741 Appendix A - 05/26/13 15:15³

742 Whole sky ETR predictions for holdout test sky 05/26/2013 15:15.

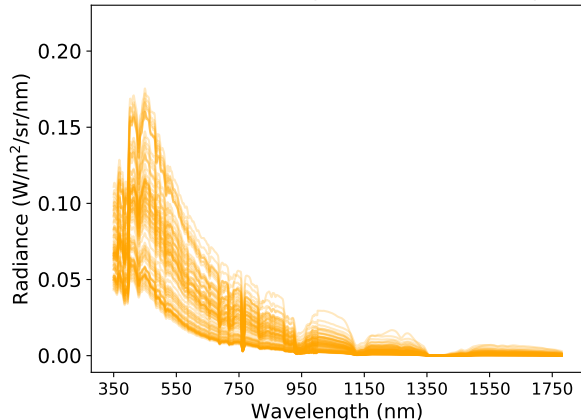
743



Measured (05/26/2013 15:15)

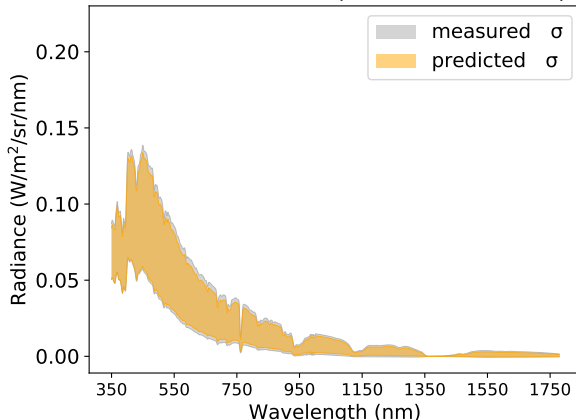


ETR Predicted (05/26/2013 15:15)

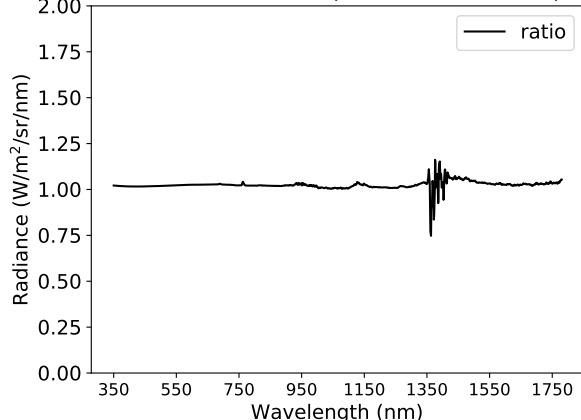


745

ETR SD from Mean (05/26/2013 15:15)



ETR Pred. / Meas. (05/26/2013 15:15)



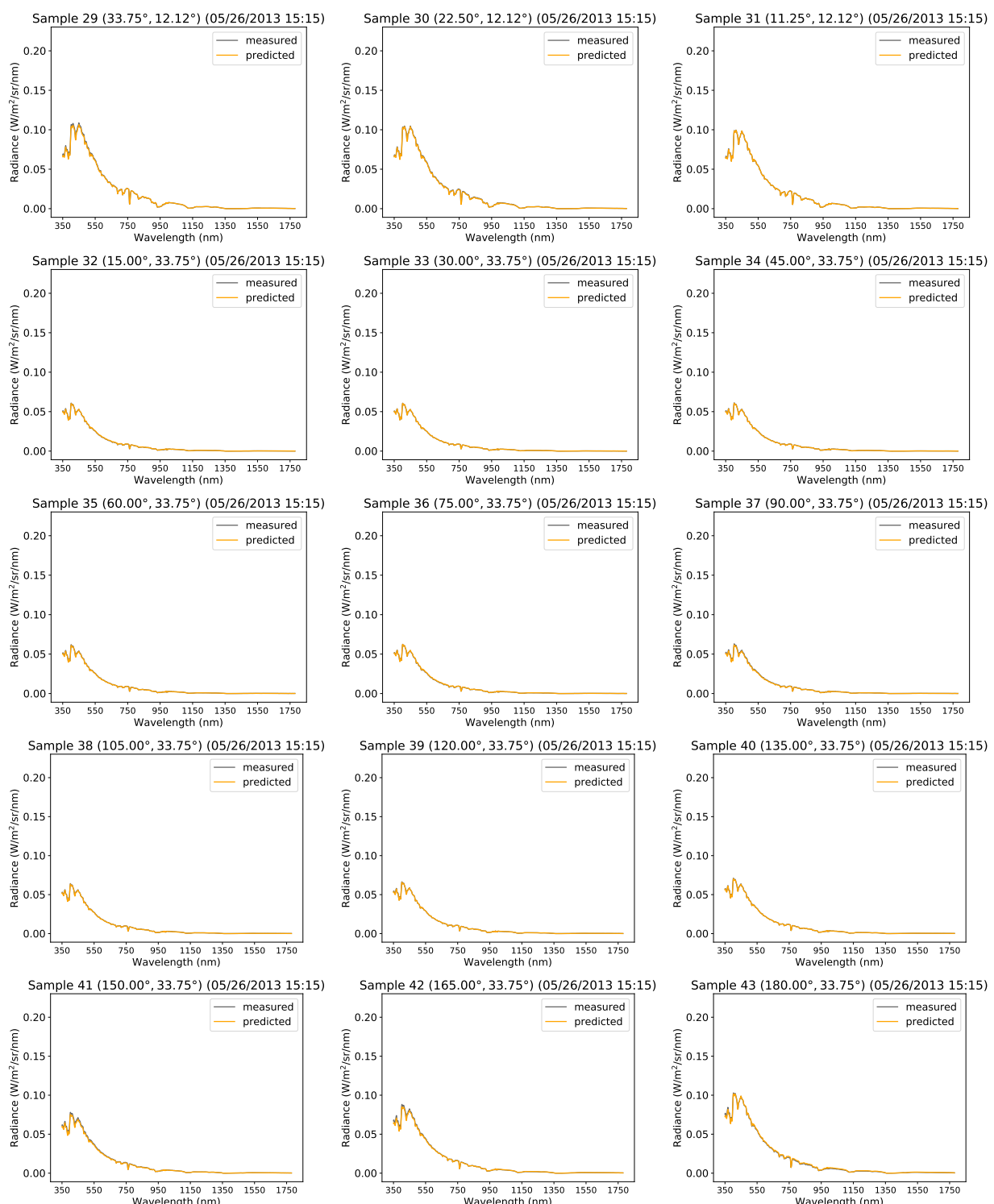
746

³Provided for reviewing purposes only.

Real-time spectral radiance estimation of clear skies

747 15 of 81 consecutive ETR spectral radiance predictions for holdout test sky 05/26/2013 15:15.

748



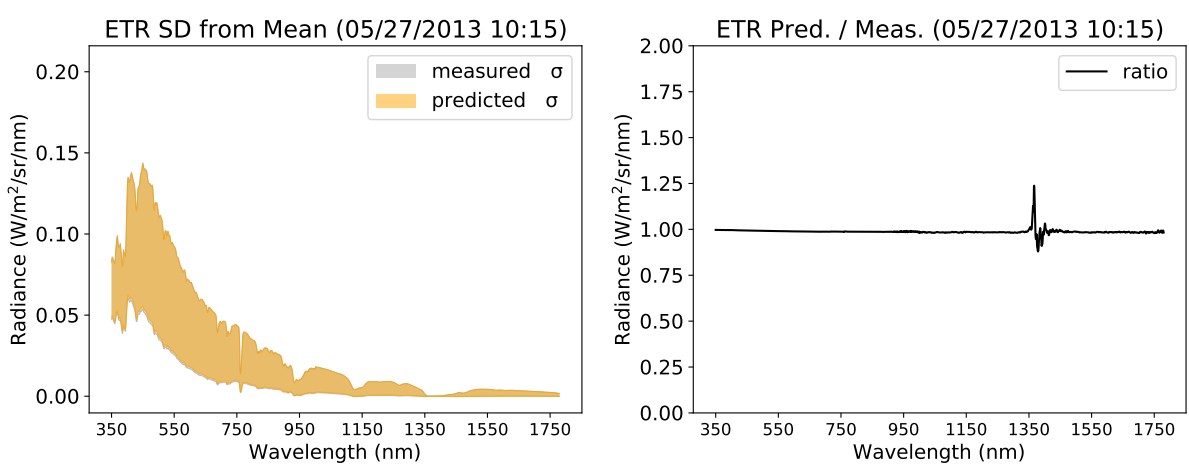
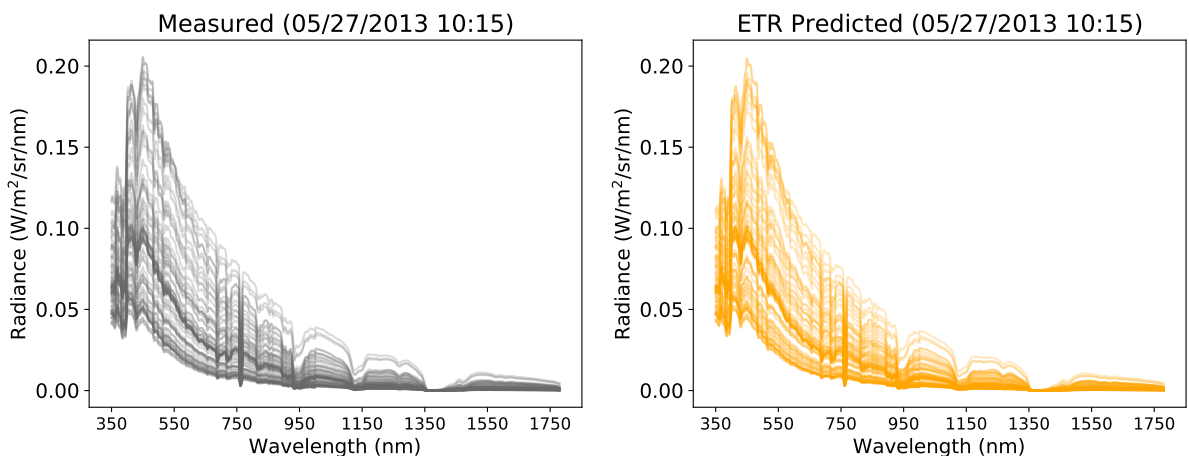
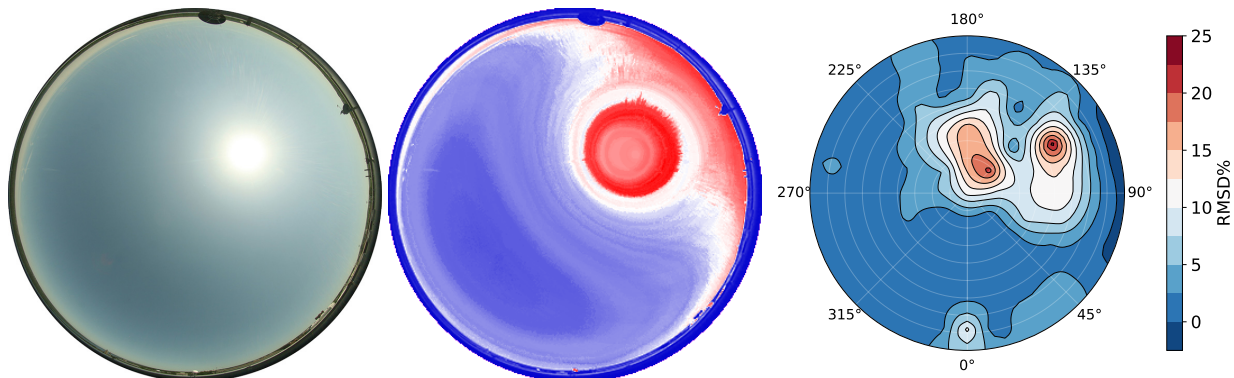
752

753

754

755 Appendix B - 05/27/13 10:15⁴

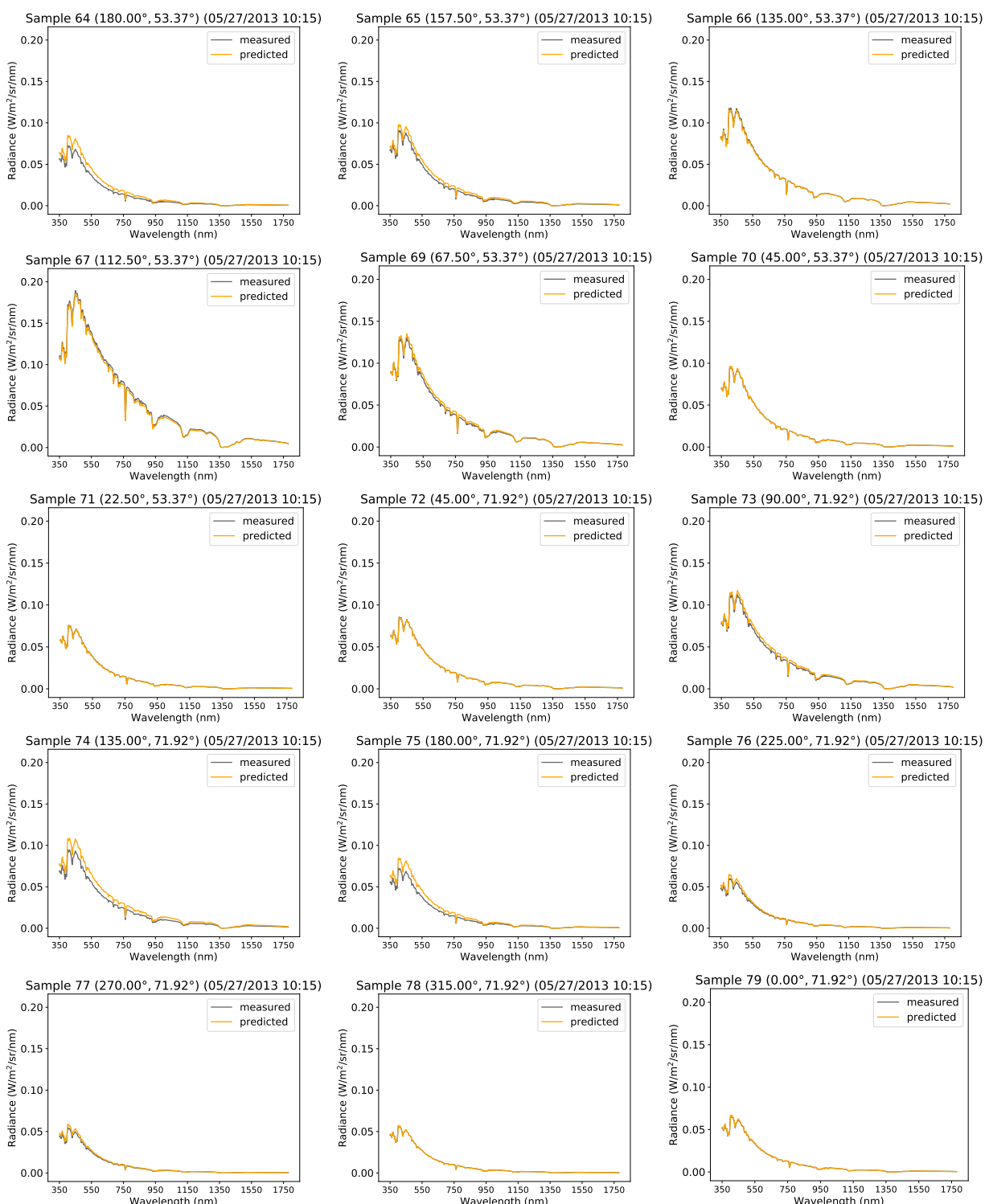
756 Whole sky ETR predictions for holdout test sky 05/27/2013 10:15.

⁴Provided for reviewing purposes only.

Real-time spectral radiance estimation of clear skies

760 15 of 81 consecutive ETR spectral radiance predictions for holdout test sky 05/27/2013 10:15.

761



762

763

764

765

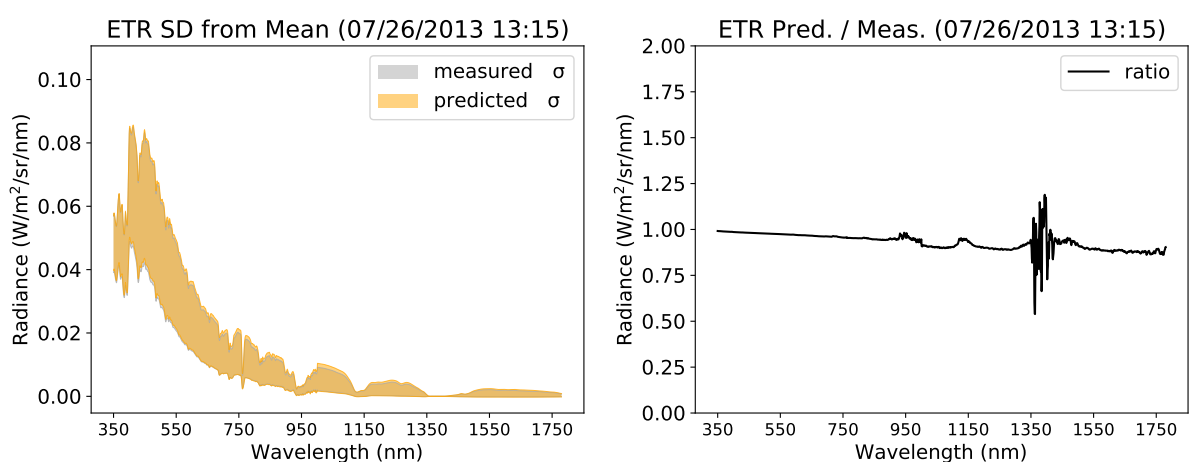
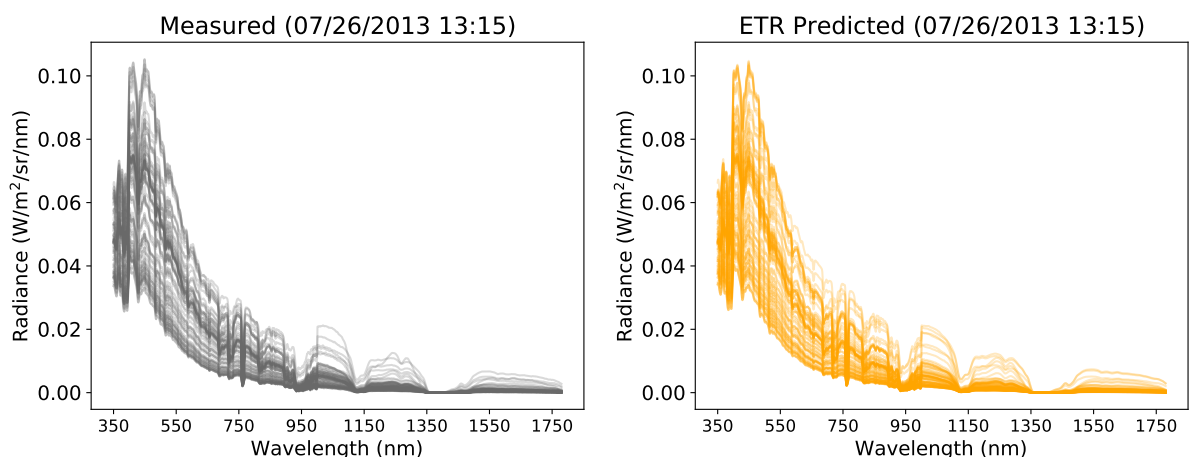
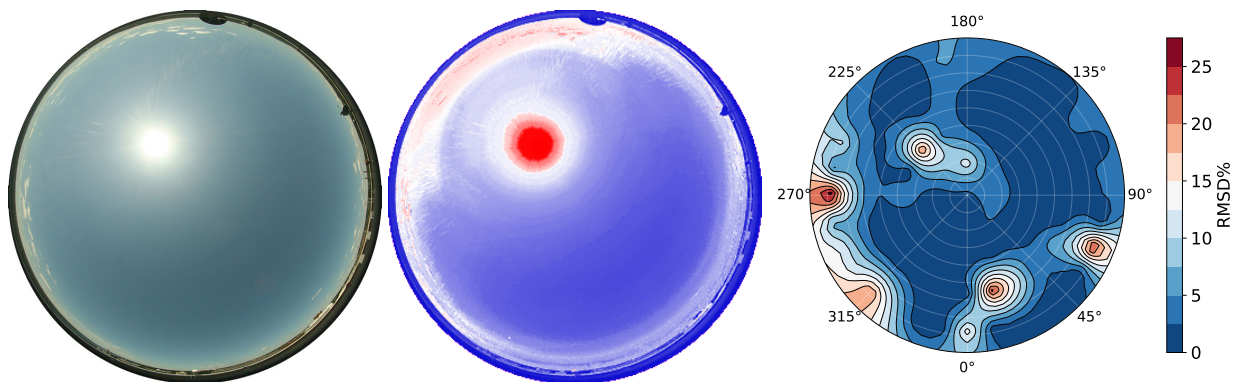
766

767

768 Appendix C - 07/26/13 13:15⁵

769 Whole sky ETR predictions for holdout test sky 07/26/2013 13:15.

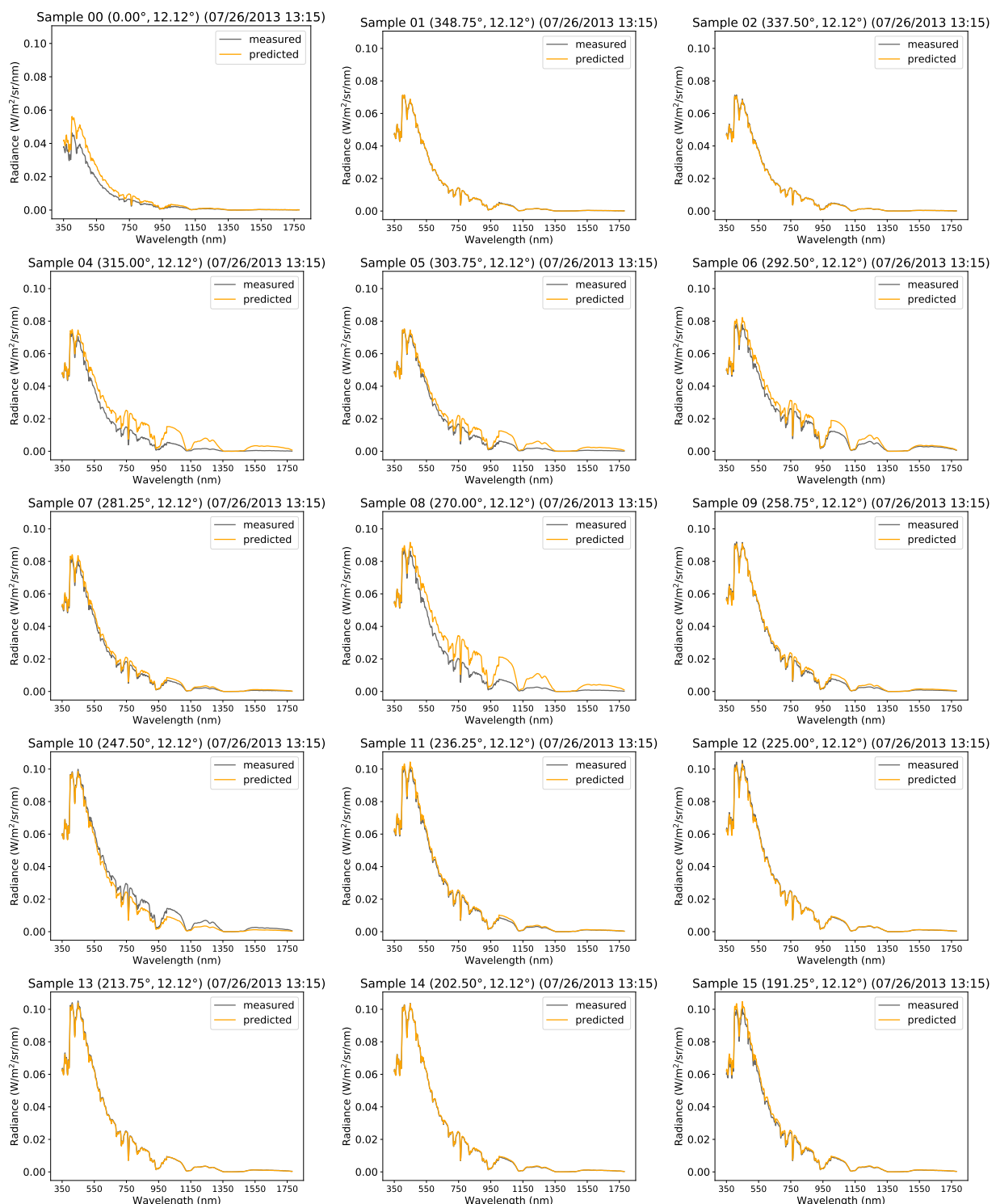
770

⁵Provided for reviewing purposes only.

Real-time spectral radiance estimation of clear skies

774 15 of 81 consecutive ETR spectral radiance predictions for holdout test sky 07/26/2013 13:15.

775



776

777

778

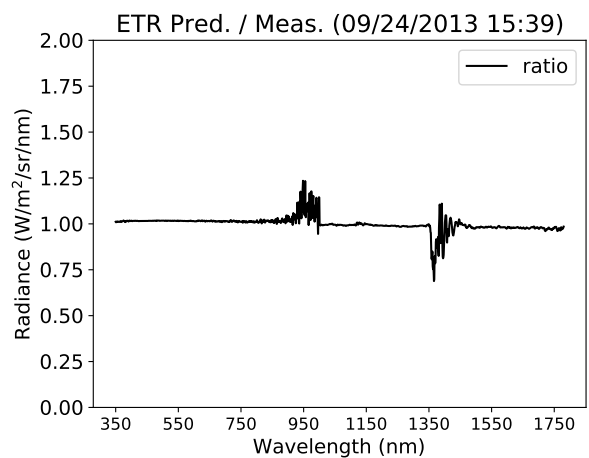
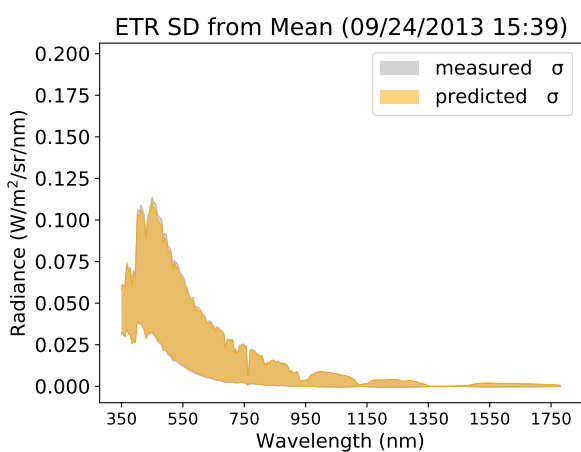
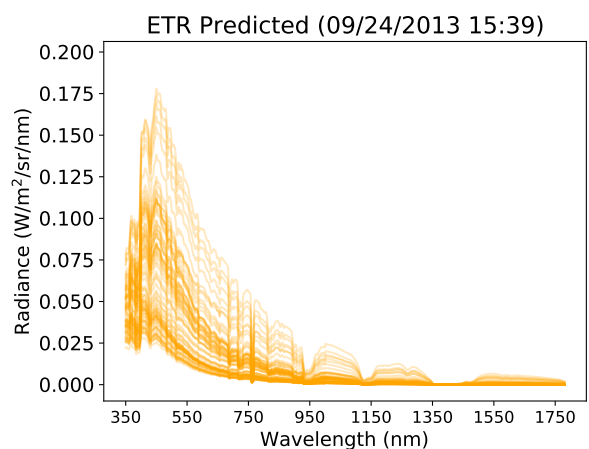
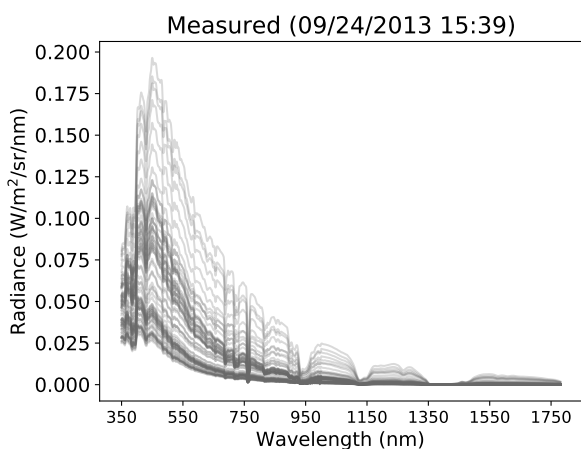
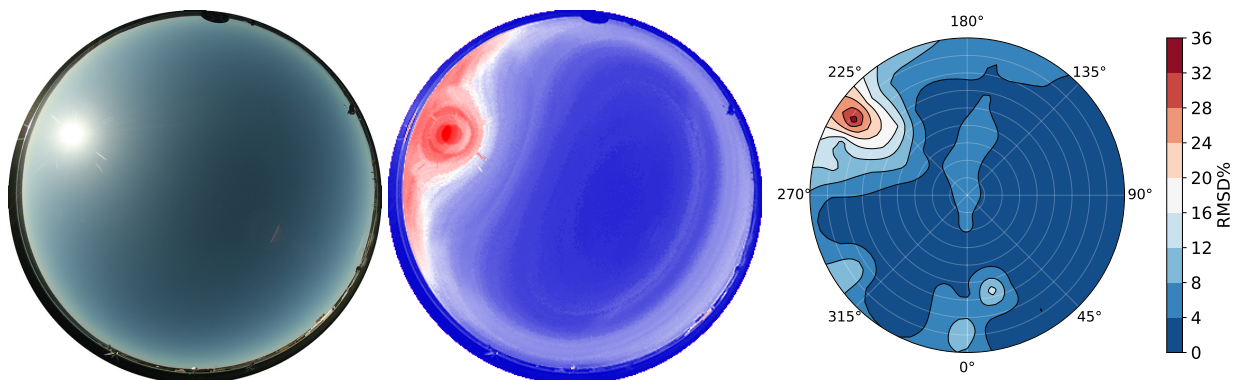
779

780

782 Appendix D - 09/24/13 15:39⁶

783 Whole sky ETR predictions for holdout test sky 09/24/2013 15:39.

784

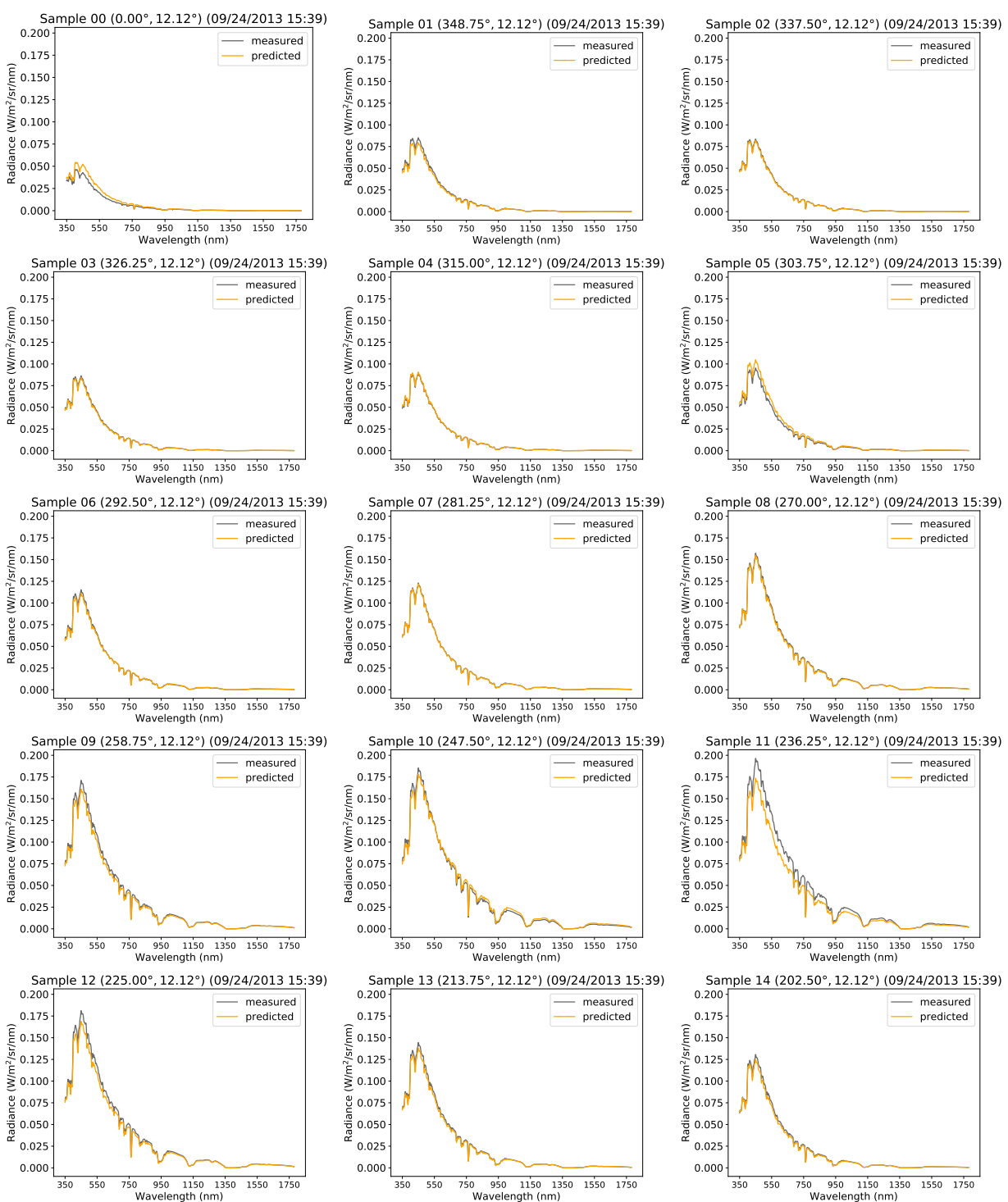


⁶Provided for reviewing purposes only.

Real-time spectral radiance estimation of clear skies

788 15 of 81 consecutive ETR spectral radiance predictions for holdout test sky 09/24/2013 15:39.

789



790

791

792

793

794

795